

A new independent look at the galactic black hole low-mass X-ray binary distribution

Y. Abdulghani,¹* A. M. Lohfink,¹ J. Chauhan^{2,1}

¹Department of Physics, Montana State University, P.O. Box 173840, Bozeman, MT 59717-3840, USA

²School of Physics and Astronomy, University of Leicester, University Rd, Leicester LE1 7RH, United Kingdom

Accepted XXX. Received YYY; in original form ZZZ

ABSTRACT

Investigations of the Galactic black hole low-mass X-ray binaries (BH-LMXBs) offer valuable insights into the elusive black hole population in the Milky Way. Motivated by recent tensions in the natal kick velocity distribution and BH mass distribution of BH-LMXBs, we revisit the spatial distribution of the Galactic BH-LMXBs using a new set of distance measurements obtained from an X-ray spectral modelling framework that we introduced in earlier work. We perform a multiparameter simulation study to mitigate part of the bias present in our prior estimates and gain insights into possible observational selection effects that affect the observed population. We derive a bias correction factor, well described by a Pareto probability density function that closely follows an inverse-square law dependence on distance. We then construct a bias-corrected, literature-independent, Galactic spatial distribution that clearly traces spiral arm structures and shows a deficit of sources very close to the Galactic centre, which might be explained due to high extinction or a true paucity of these sources at that region. Further analysis of the simulation results provides hints for a hidden population of BH-LMXBs at low Galactic heights. Lastly, we estimate the root-mean-squared Galactic height and find that it is most compatible with a hybrid scenario of BH formation, with some BHs receiving high natal kicks and thus propelled further from the thin disc plane while others receiving low natal kicks and remaining close to their birth place.

Key words: X-rays: binaries – stars: black holes – stars: distances – accretion, accretion discs – methods: statistical - Galaxy: general

1 INTRODUCTION

Low-mass black hole X-ray binaries (BH-LMXBs) are systems in which a low-mass companion star ($\lesssim 1M_{\odot}$) orbits a black hole (BH). The black hole gains mass from the companion star via Roche lobe overflow, and the accreted material forms an accretion disc (Shakura & Sunyaev 1973). These systems are predominantly detected during transient outburst events when the X-ray flux increases significantly (e.g. Remillard & McClintock 2006; Tetarenko et al. 2016). Recent increased interest has contributed to the enhanced detection of these transient X-ray binaries within our Galaxy by providing greater sensitivity and expanding sky coverage (Tetarenko et al. 2016). Despite the improved observational power, constraining the nature of the BH-LMXB population continues to present a formidable challenge.

Currently, the number of BH remnants in the Milky Way is estimated to be on the order of $\sim 10^8$ to 10^9 (e.g. Brown & Bethé 1994; Timmes et al. 1996; Samland 1998). The good detectability of BH-LMXBs in outburst makes them the leading way to study the BH population in our Galaxy. Therefore, examining the population of BH-LMXBs is crucial for gaining deeper insights into the overall BH population within our Galaxy.

The formation of BH-LMXBs is a complex issue involving stellar

evolution, dynamical modeling, and observational data (e.g. Wang et al. 2016). Several formation channels for BH X-ray binaries have been proposed (see review in MacLeod & Grindlay 2023), mostly based on well-understood binary systems. The standard model involves common envelope (CE) evolution in an isolated binary, where a massive star expands, enveloping both stars. Under certain conditions, the secondary can spiral inward, ejecting the common envelope and leading to a BH-LMXB, if the primary becomes a BH and the secondary is roughly $1 M_{\odot}$ (e.g. Ivanova et al. 2013). However, this model has been challenged, as the secondary’s low mass makes binary survival after CE unlikely (Podsiadlowski et al. 2003; Naoz et al. 2016).

Two alternative channels involving tidal capture are also considered (MacLeod & Grindlay 2023). One occurs when a wide binary dynamically encounters the primary, with the BH already formed before the capture, avoiding post-CE issues. This requires a dense environment like globular clusters or the Galactic Center (MacLeod & Grindlay 2023). The other involves a hierarchical triple system, where a tertiary’s dynamical interactions bring the secondary closer to the primary (the BH), initiating mass transfer. Though the CE phase may still happen in this case, three-body dynamics improve the chances of survival, addressing the standard scenario’s challenges (Naoz et al. 2016; Shariat et al. 2024). A supermassive black hole,

* E-mail: youssefabdulghani@montana.edu

like the one in the Galactic Center, could act as the tertiary (Lu & Naoz 2019; Hoang et al. 2022).

Regardless of the channels, the transformation of the primary from a giant to a compact star can also follow different paths; it can be accompanied by a symmetric supernova explosion, asymmetric supernova explosion or can happen with minimal mass loss, i.e. an implosion (e.g. Fryer & Kalogera 2001; Heger et al. 2003; Fryer et al. 2012). These three possibilities have significant implications for the velocity that the system may gain during the birth of the compact primary. This velocity has been widely referred to as the “natal velocity” or the “natal kick velocity”. Furthermore, the core of the primary can either collapse directly into a BH or first into a proto-neutron star and subsequently into a BH due to mass fallback (Fryer & Kalogera 2001).

Studies of the peculiar motion of a large number of neutron star LMXBs have led to strong evidence that neutron star LMXBs receive large natal kicks (e.g. Hobbs et al. 2005; Faucher-Giguère & Kaspi 2006). Several attempts have been made over the past two decades to determine whether BH-LMXBs receive equally large natal kicks (Jonker & Nelemans 2004; Repetto et al. 2012; Mandel 2016; Repetto et al. 2017). At present, both scenarios have almost the same degree of evidence, and tensions are high (MacLeod & Grindlay 2023). Nevertheless, most recently, there has been an appeal to accept a bi-modality in the natal kick distribution for BH-LMXB (Nagarajan & El-Badry 2024). Especially with the latest, very high-confidence discovery of a tertiary and low natal kick in the BH-LMXB system: V404 Cygni (Burdge et al. 2024).

The efficiency of a BH-LMXB formation channel is strongly influenced by the magnitude of the natal kick received by the system (e.g. Shariat et al. 2024). For example, the hierarchical triple formation channel generally favors a low natal velocity, as higher velocities often lead to the secondary detaching from the tertiary, thereby preventing the subsequent inward spiral (Naoz et al. 2016; Burdge et al. 2024; Shariat et al. 2024). Likewise, high natal velocities can significantly hinder the efficiency of the wide binary dynamical interaction channel, as a high-velocity BH (or neutron star) would quickly pass by a slower potential companion, preventing the energy dissipation required for tidal capture (MacLeod & Grindlay 2023).

On a related note, discrepancies between the distribution of BH masses deduced from electromagnetic observations and those inferred from gravitational wave observations (Fishbach & Kalogera 2022; Siegel et al. 2023) raise additional questions. One proposed solution to address this tension is to demonstrate that two distinct populations of BHs exist, both in turn influenced by a combination of observational and astrophysical selection effects (Fishbach & Kalogera 2022; Siegel et al. 2023). Jonker et al. (2021) pointed out that observational selection effects might explain the bias against massive BHs in the observed BH-LMXBs mass distribution. Astrophysical selection effects were also suggested to be one of the reasons behind the observed lower BH mass gap within the 2-5 M_{\odot} range in the BH-LMXB mass distributions (Özel et al. 2010; Farr et al. 2011; Kreidberg et al. 2012; Siegel et al. 2023). These selection effects could be explained in the context of natal kicks. More specifically, since mass influences natal kick velocity due to the conservation of momentum, systems with high-mass BHs and low natal velocities will be more challenging to identify observationally. Conversely, large natal kicks for low-mass BHs can disrupt the system, reducing the likelihood of BH-LMXB formation. This could introduce a selection effect where BH-LMXBs predominantly form around sufficiently massive BHs. However, it remains unclear how this explanation aligns with neutron star LMXBs, which have been shown to receive high natal kicks (e.g. Hobbs et al. 2005), despite

the assumption that the formation processes of BH and neutron star LMXBs should not differ significantly. One possible reconciliation is that if the natal kick occurs on a very short timescale (\sim tens of milliseconds), it could expel mass from the system before the proto-neutron star has time to accrete enough material to collapse into a BH (e.g. Fryer et al. 2022). However, if the natal kick occurs over a longer timescale (\sim hundreds of milliseconds), fallback accretion could still occur, leading to BH formation. This suggests that the timescale of the natal kick plays a crucial role in determining whether a compact object remains a neutron star or collapses into a BH, but further studies are needed to fully explain the observed differences (Jonker et al. 2021).

Therefore, studies of the Milky Way’s BH population are critically important in light of the recent tensions in both the natal kick distribution and the BH mass distribution. Throughout the past two decades, there have been several investigations into the population properties of BH-LMXBs in the Milky Way (e.g. Pfahl et al. 2003; Jonker & Nelemans 2004; Özel et al. 2010; van Haften et al. 2015; Repetto et al. 2017; Gandhi et al. 2020; Siegel et al. 2023; Shikauchi et al. 2023). However, past studies were inherently hampered by very small sample sizes and poor distance estimations, which were usually obtained from the existing literature.

Motivated by this lack of robust BH distribution estimates, we aim to provide a new independent examination of the Galactic spatial distribution of a relatively large sample of the observed BH-LMXBs population in this paper. Our work builds on the findings from prior work presented in Abdulghani et al. (2024, herein A24), where we developed a Bayesian framework to find dependable estimations of BH-LMXBs distance using the soft state and the soft-to-hard transition X-ray spectral modelling. Various observational and *intrinsic* properties can bias these distance estimates, which in turn could affect the spatial distribution of the observed BH-LMXB population. We thus first need to conduct extensive multi-parameter simulations that involve varying the properties and observational parameters of a synthetic BH-LMXB so that we can arrive at the characteristics of the true BH population.

This article is structured as follows: section 2 introduces the BH-LMXB simulation method and its results. Next, section 3 provides the corrected spatial distributions of the BH-LMXB in our Galaxy. We then discuss the implications of the simulations and the corrected observed distribution in section 4. Lastly, we summarise our findings and their implications in section 5.

2 OBSERVATIONAL BIAS EFFECTS ON A24’S SOFT-STATE DISTANCES: SIMULATION STUDY

To investigate the observational effects on the distances, we simulate synthetic X-ray spectra based on different observational and intrinsic properties of a hypothetical BH-LMXB that we assume is in the soft state during an outburst. We then model the simulated spectrum with a model appropriate for the soft state and obtain a best-fit as well as statistical uncertainties on the best-fit model parameters. The obtained best-fit spectral parameters are then used to constrain the source’s distance using the method developed in A24. Subsequently, by comparing the estimated distance to the distance assumed when simulating the spectrum, we can then assess the uncertainties and biases in the estimated distances arising from a particular combination of BH-LMXB properties. The resulting distance estimates will also be used to improve our understanding of the observational effects on the observed BH-LMXB population in A24.

Table 1. This table shows the parameter value set used in the spectral simulations.

Parameter (units)	Values
N_{H} (10^{22} cm $^{-2}$)	0.1, 0.5, 5, 10
D_{in} (kpc)	1, 2, 3, 4, 5, 6, 8, 12, 18, 26
Γ	1.7, 2, 3
T (keV)	0.5, 0.7, 1
a	0.0, 0.998
M (M_{\odot})	6, 8, 10
i ($^{\circ}$)	0, 60, 80
disc-to-total ratio	0.2, 0.5, 0.9
<i>MAXI</i> Exposures (sec)	400, 1500, 10000
<i>Swift</i> Exposures (sec)	400, 1000, 5000

2.1 Simulation methodology

The spectral simulations in this paper are based on the fact that the observed X-ray spectrum of a BH-LMXB can be adequately modelled to first order, with only two components that are modified by interstellar absorption; up-scattered hard X-ray emission from the hot corona believed to be present in the inner regions near the BH (Haardt & Maraschi 1991, 1993; Kara et al. 2016), and thermal emission from accretion disc (Shakura & Sunyaev 1973). While the soft state spectra of BH-LMXBs are dominated by the accretion disc component (Shakura & Sunyaev 1973), there often is also a weak continuum component present, but its strength can vary (Haardt & Maraschi 1991, 1993). In our simulations, we, therefore, vary the relative strength of the two components; this is captured in the disc-to-total ratio. In the remainder of this section, we describe the detailed method used to generate synthetic spectra of possible realisations of an observed X-ray spectrum of the soft state.

We simulated the BH-LMXB spectra in XSPEC (v12.14.1; Arnaud 1996) using the model TBabs(powerlaw+ezdiskbb). By considering different realistic combinations of the spectral model and observational parameters (Table 1), we can investigate their effect on BH-LMXB distance estimates and detection.

The disc component, modelled by ezdiskbb (Zimmerman et al. 2005), is fully determined by the maximum temperature T of the accretion disc and its normalisation. The normalisation itself is established through the distance D , inclination i , and intrinsic system properties (BH mass and BH spin). More explicitly, the normalisation can be parametrised in the following way:

$$N_{\text{ezdiskbb}} = \left(\frac{r_{\text{in}} [\text{km}]}{f_{\text{col}}^2 [D/10 \text{ kpc}]} \right)^2 \cos i \Upsilon(i) g_{\text{GR}}(a, i) g_{\text{NT}}(a) \quad (1)$$

where the $\Upsilon(i)$, $g_{\text{GR}}(a, i)$, and $g_{\text{NT}}(a)$ are correction factors based on BH spin and the inclination angle of the disc (see section 5.2 in A24 for more details). The color correction factor (or spectral hardening factor) f_{col} we assume to be approximately 1.7. The disc inner radius r_{in} , we assume, is at the ISCO, so it is a function of a and M and can be written in this form:

$$r_{\text{in}} = \frac{\zeta(a)GM}{c^2}. \quad (2)$$

where, for our purposes, $\zeta(a)$ is a multiplier that depends on the value of BH spin a (e.g. $\zeta(0) = 6$).

A simple power law is used to model the up-scattered high-energy emission. This power law is characterized by two parameters: the photon index Γ and a normalisation factor that determines the flux. In our simulations, we assume that the power law flux represents the remainder of the total unabsorbed flux after setting a specific

disc-to-total flux ratio. Additionally, to account for all possible different interstellar absorption columns along the line of sight to our simulated black hole X-ray binary in outburst, we vary the column density, N_{H} parameter, of the TBabs model (Wilms et al. 2000).

Consequently, our simulations involve selecting specific values for Γ , the disc-to-total flux ratio, the maximum disc temperature T , the inclination i , the BH mass M , and the BH spin a . Spectra are then simulated for all possible combinations of these parameters. One of our main goals from the simulations is to correct the biases intrinsic to the instruments, which are present in the A24 distance estimations. So, the parameter values considered in the simulations were chosen primarily based on the observed ranges in the A24 spectral modelling results, and the priors on BH properties we used in A24. We also aimed to explore fiducial combinations while allowing for a few edge cases. For example, we selected three Γ values, 1.7, 2, and 3, since typical soft-state values lie between $\Gamma = 2$ and $\Gamma = 2.5$ (Remillard & McClintock 2006); the $\Gamma = 1.7$ case accounts for a harder-than-usual spectrum, while $\Gamma = 3$ represents a softer-than-usual scenario.

Moreover, we chose three values for the maximum disc temperature, $T = 0.5, 0.7,$ and 1 keV (e.g. Muñoz-Darias et al. 2013), two values for the BH spin, no-spin $a = 0$, and maximal-spin $a = 0.998$ (Reynolds & Miller 2013), and three values for the BH mass, $M = 6, 8,$ and $10 M_{\odot}$ (Özel et al. 2010). We also considered three values for the disc-to-total flux ratio, 0.2, 0.5, and 0.9 (Remillard & McClintock 2006) and selected three disc inclination values that span the minimum ($i = 0^{\circ}$), expectation value ($i = 60^{\circ}$) and near the possible maximum ($i = 80^{\circ}$). We adopted three values for each instrument for the exposure time, based on the values observed when analysing the A24 sample.

In addition to these parameters, we implemented non-uniform grids for the distance and N_{H} values. Specifically, we constructed a 4-by-10 $D_{\text{in}} - N_{\text{H}}$ grid that covers distances likely to occur within the Galactic sample and spans the typical N_{H} values up to the ‘‘maximum’’ value (HI4PI Collaboration et al. 2016). Table 1 presents the full set of simulation parameters for each instrument.

The spectra simulation were performed using the *fakeit* command in XSPEC. Spectra are generated based on the predetermined set of model parameters. The simulation procedure was conducted using representative background and response files from both Neil Gehrels Swift Observatory/X-ray Telescope - Windowed Timing mode (*Swift*/XRT-WT data; Gehrels & Swift 2004) and the Monitor of All-sky X-ray Image/Gas Slit Counter (*MAXI*/GSC; Matsuoka et al. 2009). We binned the simulated spectra to a signal-to-noise ratio (SNR) of 3, consistent with the data reduction methodology used in A24. We do not take into account in our simulations the *Swift*/XRT pile-up effects (Mineo et al. 2006) that affect sources with high flux (≥ 100 counts s $^{-1}$) (Romano et al. 2006), since we assume that the simulated spectrum would be the resulting spectrum after correcting for pile-up.

The generated spectra have random Poisson errors, to ensure that we get a representative sample of the simulated spectra, each simulation was repeated 300 times. However, to provide a concise synopsis of the modelling results of the 300 simulated spectra per parameter combination, we calculated the weighted median of the estimated distances after generating the 300 spectra. The weight is constructed from the mean fractional uncertainty by utilising lower and upper 90% confidence bounds of the ezdiskbb normalisation parameter. The 90% confidence bounds of the ezdiskbb normalisation for each simulated spectrum were calculated using XSPEC’s *error* command.

The mean fractional uncertainty is thus taken to be $f_{\delta} = (D_{\text{est,upper}} - D_{\text{est,lower}})/D_{\text{est,best-fit}}$ so that the weight is $w = 1/f_{\delta}$.

Moreover, the weighted median of the 300 simulations was taken to be the quoted estimated distance D_{est} for that parameter combination.

We also evaluated whether a source was too faint at certain parameter combinations to obtain a distance estimate via this spectral method. Specifically, if the simulated spectrum is of such low quality that the number of data points in the binned ($\text{SNR} \geq 3$) spectrum is less than the number of fit parameters, we consider the source “undetectable” for that combination.

In summary, the simulation procedure was as follows:

- (i) For each grid point in the $4 \times 10 D_{\text{in}}-N_{\text{H}}$ grid, simulate 300 spectra with random error
- (ii) Repeat step 1 for each of the 1,458 combinations of the other parameters listed in Table 1. This results in a total of 17,496,000 simulated spectra per instrument for each input parameter combination
- (iii) Reduce these 17,496,000 spectra per instrument to 58,320 by computing the weighted median (as described above) of the 300 repeated simulations for each combination
- (iv) Use these 58,320 combinations per instrument as the starting point for all subsequent results presented below

2.2 Simulation results

A total of 34,992,000 simulations were generated. The computations were performed on the MSU-Tempest HPC research cluster¹ and consumed around 17,000 CPU hours. Since the results of the simulations are extremely large, it is intractable to look at every possible simulation parameter combination. Therefore, we focus our investigation on three avenues. We begin by examining how the deviation from the input distance varies as a function of the input distance for each of the eight simulation parameters (Section 2.2.1). We then probe important pairwise parameter interactions through a Bayesian Information Criterion (BIC) selection process (Section 2.2.2). Finally, we provide a holistic view of the estimated distance distributions, to utilise these distributions as bias correctors.

2.2.1 Effects of individual parameters

We first look at the effects of every individual parameter on the estimated distance. We examine the effects by calculating the deviation of each estimated distance from the input distance $\Delta D_{\text{est,in}} = D_{\text{est}} - D_{\text{in}}$ for each parameter combination. Then, for each parameter (e.g., Γ with input values 1, 7, 2.0, 3.0), we calculate the median of the deviations across the different input values of the parameter. The resulting median $\Delta D_{\text{est,in}}$ thus provides an overall estimate of the error on the estimated distances for a given input parameter. In Figure 1, we show the effects of N_{H} , Γ , T , and a on the deviations from the input distance for the estimated distances from *MAXI/GSC* (left plot) and *Swift/XRT* (right plot) simulations. The results from both instruments show a general trend of higher negative deviation (estimated distance is less than the input distance) as the input distance increases. However, we note that there is one exception to this, the $\Gamma = 1.7$ simulations (top-right panel in the right plot of Figure 1) in the *Swift/XRT* results, which shows an increase in the median positive deviations.

Comparing the results of *MAXI/GSC* with those of *Swift/XRT*, we observe that the changes in the deviation with increasing input distance are steeper for *MAXI/GSC*. However, the $a = 0.998$ case is an exception to this general trend, which shows a more sudden drop

in the *Swift/XRT* estimated distance for the highest distance value (26 kpc). Looking at the impact of the individual parameters on the accuracy of the estimated distances, we note that higher N_{H} values (Figure 1, top-left panel) affect *MAXI/GSC* more than *Swift/XRT*. We also note that the change of the accretion disc maximum temperature T (Figure 1, bottom-left panels) does not affect the median deviation of *Swift/XRT* results as much as their *MAXI/GSC* equivalents.

Similarly in Figure 2, we show the effects of M , i , disc-to-total ratio, and exposure time. The general trend remains the same, where we observe an increasing negative deviation with increasing distances, with the exception of the disc-to-total ratio 0.9 in the *Swift/XRT* simulations. The *MAXI/GSC* deviations show stronger changes for all of these four parameters. We underscore that the exposure and black hole mass changes do not affect the median error of the *Swift/XRT* simulations as much as they affect the *MAXI/GSC* ones.

It is important to note here that the median deviation results only show the general trends of the central tendency of the estimated distance. However, they do not capture the full picture of the estimated distance results. Thus, we also investigated the kernel density estimations (KDE) distributions of the deviations. To facilitate examining the differences more easily, we take the log-modulus transformation (John & Draper 1980) of the deviation $\Delta D_{\text{est,in}}$ (Equation A1). This transformation preserves the sign of the deviation while taking the log of the deviation, which helps compress the plotting range and makes the plot easier to read. Figures A4–A8 in the appendix show the KDE distributions for all eight parameters. For brevity, we concentrate here on the most important findings that we can draw regarding the distributions from the KDEs. The *Swift/XRT* error distributions appear to be wider with less pronounced peaks and some bi-modalities than those from *MAXI/GSC*. However, the distributions’ central values appear closer to zero (i.e. the error is lower). In contrast, the *MAXI/GSC* distributions are narrower with well-defined single peaks tending toward larger negative deviations (input distance is more underestimated). A more comprehensive and detailed discussion about the error distributions can be found in appendix A.

2.2.2 Pairwise interaction effects between parameters

Having examined individual parameter effects, we further try to understand how the parameters are entangled by studying the interaction between parameter pairs, which can affect the ability of the method to recover input distance.

We explore the pairwise interactions between the eight parameters (N_{H} , Γ , T , a , M , i , disc-to-total ratio, exposure time) that affect the estimated distance distribution. But to avoid investigating all 28 combinations of the pairwise interactions for both instruments, we first determine which interactions are important through a Bayesian Information Criterion (BIC; Schwarz 1978) backward stepwise process. In particular, we model the estimation of fractional uncertainty

$$\frac{|\Delta D_{\text{est,in}}|}{D_{\text{in}}} = \frac{|D_{\text{est}} - D_{\text{in}}|}{D_{\text{in}}} \quad (3)$$

using a linear model that contains all the pairwise interactions of the eight parameters, the main effects of the parameters, as well as the input distance as an additive component to control for the change in the input distance. For this modelling process, we only consider estimates with a fractional uncertainty $\left(\frac{|\Delta D_{\text{est,in}}|}{D_{\text{in}}}\right) \leq 1$ (100%). This was done because we would like to study only the relative magnitude of the interactions, so obtaining a model that fits the whole dataset was unnecessary. Additionally, the outliers complicate the modelling pro-

¹ <https://www.montana.edu/uit/rci/tempest/>

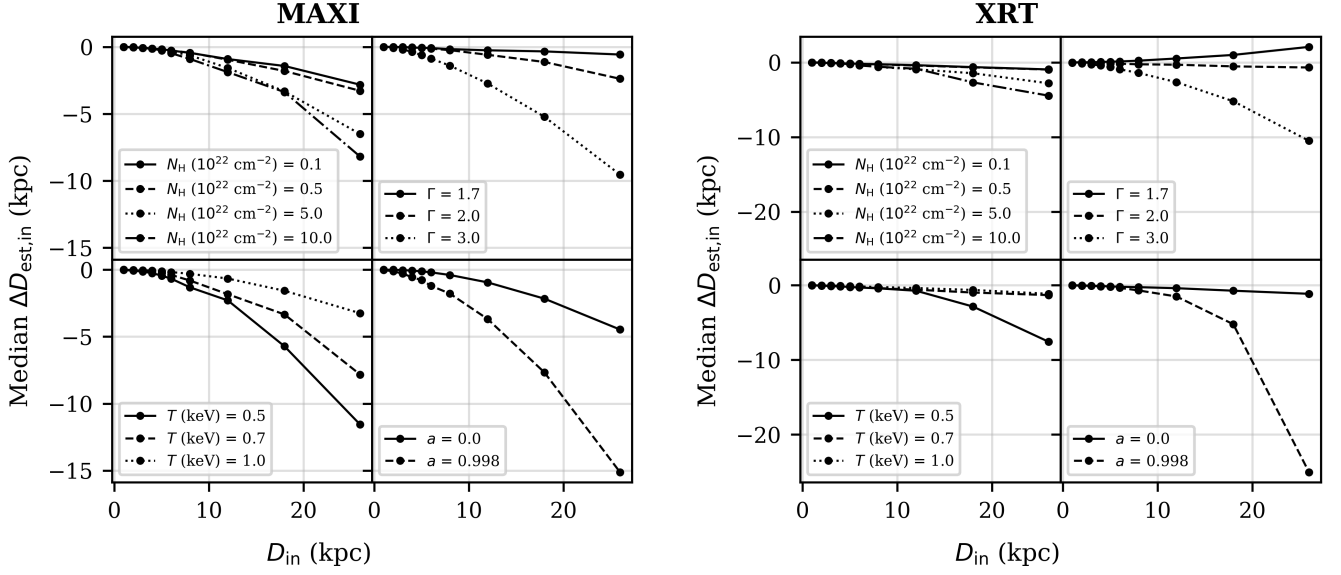


Figure 1. The plot highlights the median difference between the estimated distance and the input distance ($\Delta D_{\text{est,in}}$) as a function of input distance (D_{in}). We present $\Delta D_{\text{est,in}}$ vs D_{in} variation for the different values of: N_{H} (top-left), Γ (top-right), T (bottom-left), a (bottom-right). **Left.** Shows the results for MAXI/GSC simulations **Right.** Shows the results for Swift/XRT simulations.

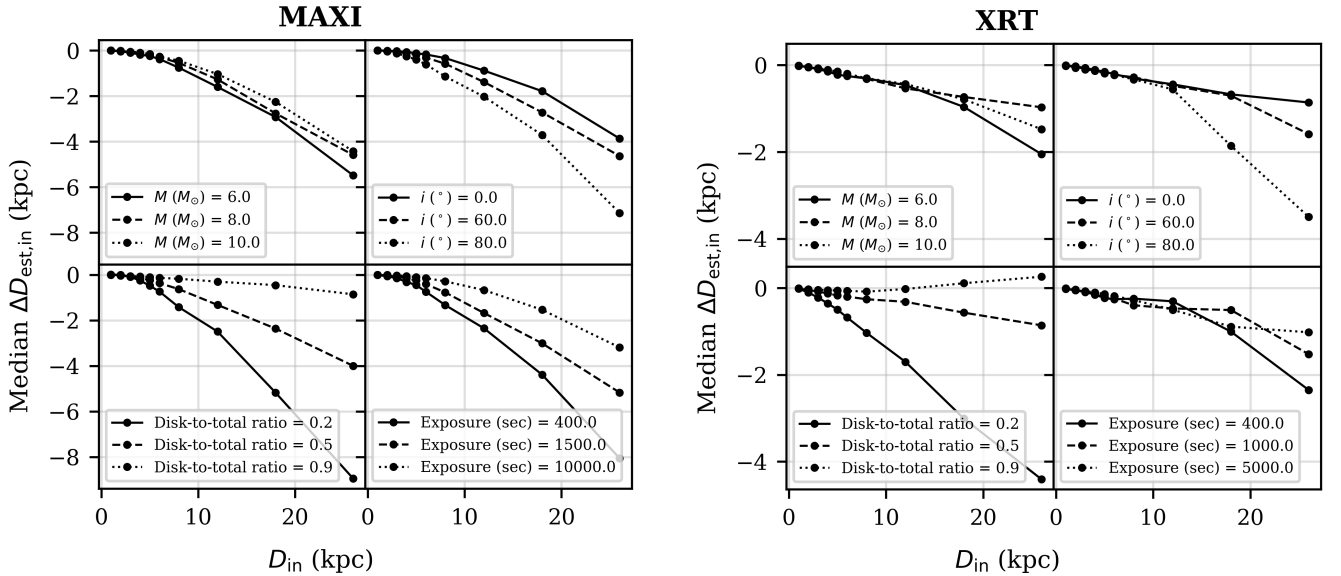


Figure 2. Same as Figure 1 but for: M (top-left), i (top-right), disk-to-total ratio (bottom-left), Exposure time (bottom-right). **Left.** Shows the results for MAXI/GSC simulations **Right.** Shows the results for Swift/XRT simulations.

cess, but should not considerably affect the conclusions, especially concerning the importance of an interaction effect.

We take the log of the fractional uncertainty, since it makes the residual distribution follow the assumed normal distribution more closely, which significantly enhances the diagnostics of the models and consequently strengthens the validity of our conclusions. However, we have transformed back to fractional uncertainty (as a percentage) when we present the interaction plots (Figures 3, 4, and 5) to ease interpretation.

In the BIC stepwise process, we start by using the full model,

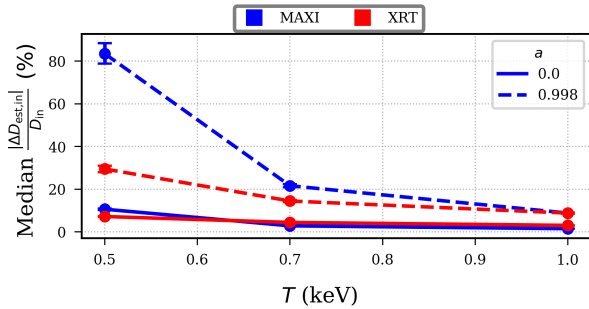
which contains all 28 pairwise interactions, then iteratively subtract interaction terms and calculate the BIC; if the BIC is lower than before, we take that reduced model as the current model. We then repeat this process until we reach a model where subtracting any interaction terms results in an increase in the BIC.

The final model obtained after using this process for MAXI/GSC is the model where we have 13 interactions as listed in Table 2. In contrast, for the Swift/XRT simulations, the backward step process yielded the lowest BIC model with 11 interactions (Table 2).

We observe that the interactions mostly follow the same patterns

Table 2. Interactions included in the final models for *MAXI/GSC* and *Swift/XRT* simulations.

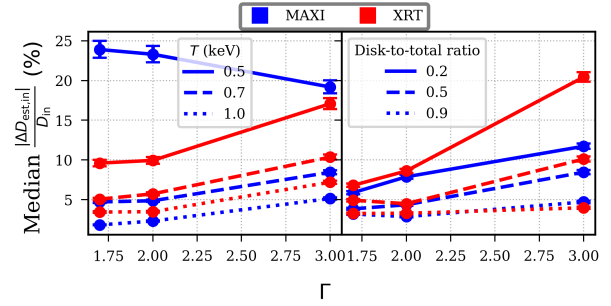
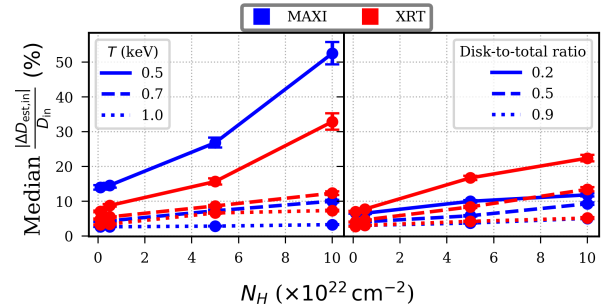
	a	i	T	Γ	Exposure	disc-to-total ratio
<i>MAXI/GSC</i>						
a		✓			✓	
T	✓				✓	✓
Γ	✓		✓		✓	✓
N_{H}	✓		✓	✓		✓
<i>Swift/XRT</i>						
a		✓				
T	✓					✓
Γ	✓		✓		✓	✓
N_{H}	✓		✓	✓		✓

**Figure 3.** This figure shows the important pairwise interaction between the maximum disc temperature T and the BH spin a . This was one of the interactions selected via the backward stepwise BIC process.

as in the individual parameter effects (see previous section). Thus, we succinctly show the most interesting interactions in this section while providing the rest of the BIC-selected interaction effects plots in appendix B.

Building on these observations, we now focus on a key interplay between the maximum disc temperature T and the BH spin a , which offers further insight into the models' behaviour. In Figure 3, we plot the $T:a$ interaction. The figure shows that the increase in temperature when the BH is not spinning does not affect the relatively low median fractional uncertainty. In contrast, we observe that the increase from a disc temperature of 0.5 keV to 1 keV substantially improves the median fractional uncertainty of the high-spin simulations, especially for *MAXI/GSC*. It is also to be noted from this figure and the rest of the interaction plots that the overall highest median fractional uncertainty from this model is obtained when $T = 0.5$ keV and $a = 0.998$ with *MAXI/GSC* having a median fractional uncertainty of $\sim 80\%$ at that combination, while *Swift/XRT* having a median fractional uncertainty $\sim 30\%$.

Another interesting interaction is the $\Gamma:T$ one, as shown in the left panel of Figure 4. Here, the average fractional uncertainty generally increases with increasing Γ and decreasing T . However, we observe an exception to this trend for *MAXI/GSC* results and the lowest temperature case, where at the highest Γ , we have a considerably lower fraction uncertainty. This ‘‘anomalous’’ decrease in the average fractional uncertainty for the highest Γ and lowest T is not present in the $\Gamma:T$ results for the *Swift/XRT* simulations, which shows a consistent trend. In the right-hand panel of Figure 4, the Γ :disc-to-total ratio interaction is shown. The plot provides an intriguing result, where we see that for *Swift/XRT*, the combination of high

**Figure 4.** This figure shows the important pairwise interactions between the Γ and other parameters. These interactions were selected via the backward stepwise BIC process.**Figure 5.** This figure shows the important pairwise interactions between N_{H} and other parameters. These interactions were selected via the backward stepwise BIC process.

disc-to-total flux ratio and high Γ increases the fractional uncertainty substantially.

We observe another noteworthy finding in the $N_{\text{H}}:T$ interaction (left-hand panel of Figure 5). At disc temperatures of $T = 1$ keV and 0.7 keV, the median fractional uncertainty changes minimally as the amount of absorption N_{H} increases. Conversely, we observe that variations in the median fractional uncertainty exhibit more abrupt transitions at the lowest temperature.

The last interesting interaction effect we mention is the $N_{\text{H}}:$ disc-to-total ratio, where the fractional uncertainty of the *Swift/XRT* simulations shows a clear positive trend with increasing ratios and absorption. In contrast, the *MAXI/GSC* median fractional uncertainty shows a significantly weak positive trend.

Figures B1-B6 in the Appendix show all remaining interactions and their effect on the median fractional uncertainty.

As clear from the final BIC-selected models presented before, unlike the *MAXI/GSC* simulations, the a :Exposure and T :Exposure interactions were deemed unimportant by the BIC process for *Swift/XRT*. Generally, we notice that the median fractional uncertainties for *Swift/XRT* at the worst combinations are generally less than the *MAXI/GSC* results, except in a few cases, namely the $N_{\text{H}}:$ disc-to-total ratio, Γ :disc-to-total ratio, and $N_{\text{H}}:\Gamma$, where we find that the magnitude of the median fractional uncertainties are higher than their *MAXI/GSC* counterparts.

2.2.3 Overall distance recovery distributions

To summarise our results, we show stacked histograms (Figure 6) of the number of simulations per input distance with an estimated

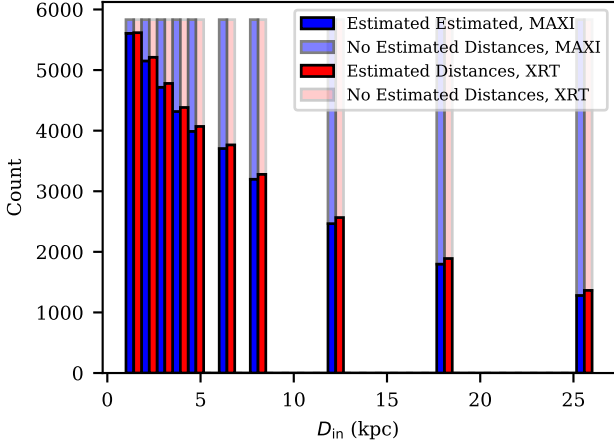


Figure 6. This plot shows a stacked histogram of the availability of distance estimations. This illustrates the overall ability of the instrument to provide a spectral fit that is sufficient to permit distance estimation. Note that for each D_{in} we have a total of 4 (for each N_{H} value) $\times 1458 = 5832$ simulations.

distance and the number of simulations input distances without an estimated distance. The lack of an estimated distance occurs due to the very low number of bins in the simulated spectrum, i.e. a low SNR in the spectrum. As expected, the number of available distance estimates appears to decay exponentially with increasing distance. While for *MAXI/GSC*, at the lowest distance, we have almost all of the simulated spectra (96%) yielding a distance estimate. At the highest distance, only 1280 out of 5832 (22%) simulations yield an estimate for the distance. In contrast, the decay in the number of estimable distances for *Swift/XRT* is slightly shallower. For example, looking at the number of the estimable distance at $D_{\text{in}} = 26$ kpc, we observe a marginally larger number in the case of *Swift/XRT* compared to *MAXI/GSC*, with a count of 1364 as opposed to 1280 distances.

Restricting the estimated distances to only those with less than 50% error from the input distances, we obtain empirical bias distributions of whether a fictitious source at a certain input distance could yield a distance estimate with error less than 50% of the input distance. We convert these distributions to a probability density and model the density using possible candidate functions (Table C1). We found that the function with the lowest mean squared error has power-law-like behaviour, in particular, the Pareto probability density function (PDF), which has the following form:

$$f(D_{\text{in}}) = \frac{b}{(D_{\text{in}} - c)^{b+1}} \quad (4)$$

For *MAXI/GSC* the best-fit parameters were found to be: $b = 0.79 \pm 0.043$, $c = -12.88 \pm 0.45$. On the other hand, the best-fit parameters for *Swift/XRT* are: $b = 0.87 \pm 0.098$, $c = -14.62 \pm 1.075$. The normalised Pareto PDFs for both instruments are shown in Figure 7. We note how close both distributions are to each other; we also observe that both distributions are approximately proportional to the usual radiation inverse squared law relation $1/D^2$. With some offset in D . Since the PDFs from *MAXI/GSC* and *Swift/XRT* are almost identical, we take the average values of the best-fit values of both PDFs. We then use that in the next section (Section 3) to correct the observed distance distribution obtained using the soft-state method in A24.

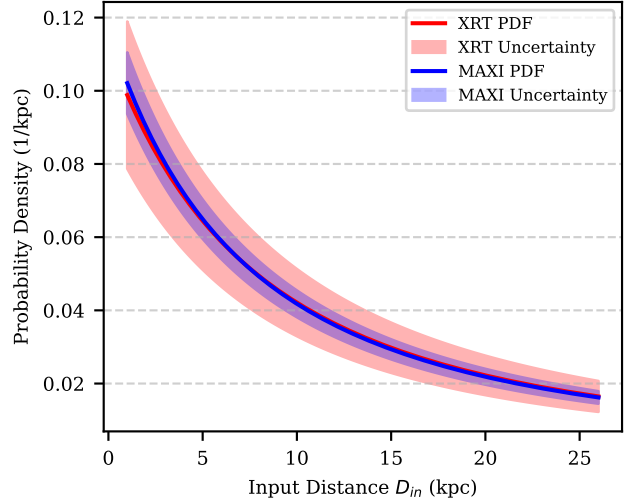


Figure 7. This figure shows the re-normalized fitted Pareto distributions to the density distribution of estimated distances that are within 50% error of the input distance. The red curve is for *Swift/XRT*, and the blue curve is for *MAXI/GSC*. These distribution shows the overall ability of the instruments to provide accurate (within 50%) distance estimations when using the soft-state method. The shaded regions correspond to the $1-\sigma$ uncertainties from the curve fitting procedure. The fitted PDFs are very close to an inverse square law relation ($\propto 1/D^2$). Figure best viewed in colour.

3 THE CORRECTED OBSERVED SPATIAL DISTRIBUTION

In the previous section, we estimated the systematic biases of the instruments using the soft-state model discussed in A24. We proceed to leverage this biased assessment to mitigate some aspects of the systematic error that was present in our soft-state A24 estimates. We “correct” the bias by dividing the observed distance distribution from the soft state by the average PDF found in the last section. We then use the de-biased distance estimates to create a picture of the galactic spatial distribution of BH-LMXBs.

As A24’s sample included sources observed by the Rossi X-ray Timing Explorer/Proportional Counter Array (*RXTE/PCA*; Bradt et al. 1993) in addition to *MAXI/GSC*, and *Swift/XRT*. Therefore, we also want to apply our bias correction to the *RXTE/PCA* distributions from A24. We note here that to avoid performing additional computationally expensive simulations for *RXTE/PCA*, we assume that our average bias PDF obtained from the *MAXI* and *Swift* simulations applies to *RXTE/PCA*. Although the response of *RXTE/PCA* to the X-ray background will differ somewhat from *MAXI/GSC* and *Swift/XRT*. We believe it is most likely to have a similar bias profile with distance. Firstly, because the energy range we used in A24 for *RXTE/PCA* is 3–20 keV, almost identical to the 2–20 keV range used for *MAXI/GSC*. Additionally, the effective area of only one² of the proportional photon counters (PCA) is around 1300 cm² which is in between *MAXI/GSC*’s (~ 6500 cm²) and *Swift/XRT*’s (~ 100 cm²) effective areas (Bradt et al. 1993; Matsuoka et al. 2009; Gehrels & Swift 2004). Finally, we expect the profile to be proportional to $1/D^2$ (see discussion section 4.1).

In the A24 study, we presented a heliocentric distance distribution of all BH-LMXBs (Figure 3 in A24) by adding the best estimates of

² We only used Proportional Counter Unit (PCU) 2 in A24.

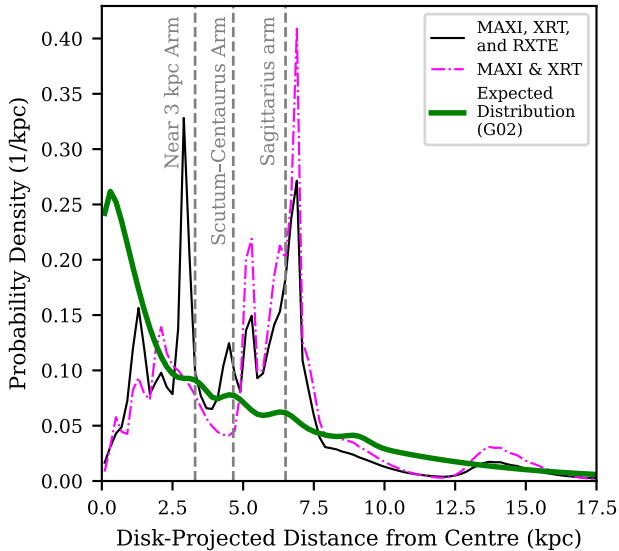


Figure 8. This plot shows the corrected and aggregated probability distribution of disc-projected Galactocentric distances using the *MAXI* and *Swift* sources (magenta line) and when including *RXTE* sources (black line). The expected distribution from (Grimm et al. 2002) (green line) is also shown. The vertical dashed lines mark the approximate locations of the near 3 kpc Arm, the Scutum–Centaurus Arm, and the Sagittarius Arm (Reid et al. 2019). This figure is best viewed in colour.

individual source distributions. In this current study, we improve this heliocentric distance distribution by utilising the corrected distribution and transforming the heliocentric coordinates to Galactocentric ones. In Figure 8, we show the disc-projected Galactocentric distance probability distribution as observed by *MAXI* and *Swift* with the magenta curve. When we also extrapolate our bias corrector to the *RXTE* sources, we show the corrected distribution with the black line. The distribution with all three detectors shows peaks at ~ 1.5 kpc, 2.9 kpc, followed by a dip in the 3–4 kpc range. This is followed by a double-peaked structure around 5 kpc. The density increases rapidly in the 6.5–7.5 kpc region. Lastly, an elevated density is visible in the 12.5–15 kpc range. The distribution with only *MAXI* and *Swift* estimations displays the same major features but shows more a stair-like increase in the density in the 0–2.5 kpc range and more pronounced dip in the 3–4 kpc range.

Using the best (lowest 1σ errors) bias-corrected median distance estimate we obtained for each of the sources as well as their right ascension and declination, we produced a histogram of the absolute galactic heights $|z|$ (Figure 9). Again, we separate the *MAXI* and *Swift* distribution from the one in which we include all detectors. Both histograms show that almost all sources in our sample have absolute galactic heights between 0.2 and 0.8 kpc, with only 3 sources having an absolute galactic height ≥ 1 kpc.

Furthermore, we adopt the right panel of Figure 1 in Jonker et al. (2021) and construct a similar graph of $|z|$ against the disc-projected Galactocentric distance (Figure 10).

The figure shows that the sample’s Galactic heights are mostly contained in the region between 60 pc and 1000 pc. However, few sources appear to have higher or lower Galactic height by a factor of $\sim 2 - 3$.

Finally, for completeness, we provide an updated 2D map of the sources on the Milky Way plane in Figure D1. We found that our general observations from A24 remain unchanged, where most sources

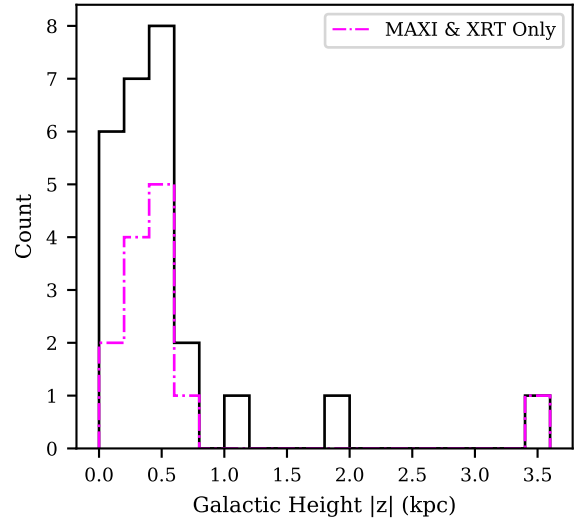


Figure 9. This plot shows a histogram (bin width = 0.2 kpc) of the absolute galactic height $|z|$ for the 20 sources in our sample using the best (with lowest $1-\sigma$ errors) median distance estimates we obtained for each of them. The magenta line corresponds to *MAXI* and *Swift* sources only, and the black line corresponds to the results when including *RXTE* source. The `astropy.coordinates` method was used to transform the (ICRS frame) RA, dec, and the distance into the galactocentric coordinates (ρ , ϕ , z). The distance of the sun from the Galactic Centre was set to 8.122 kpc, and the height of the Sun from the disc is 20.8 pc (Bennett & Bovy 2019). This figure is best viewed in colour.

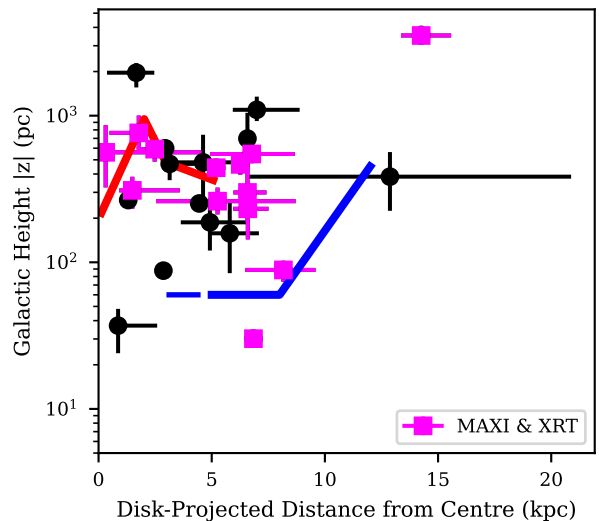


Figure 10. The plot shows the absolute galactic heights of our sample $|z|$ as a function of the disc-projected Galactocentric distance. This figure is adapted from the right panel of Fig. 1 in Jonker et al. (2021). The red line approximates the shape and height of the Galactic Bulge (Portail et al. 2015; Wegg et al. 2015). While the blue line is 3 times the 20 pc scale height of massive stars in the region between 5 and 8 kpc from the galactic centre (Urquhart et al. 2014; Reid et al. 2019). Following Jonker et al. (2021), we extend the line to the lower distance of 3 kpc. While for larger distances between 8 kpc and 12 kpc, the scale height increases quickly to 450 pc. This figure is best viewed in colour.

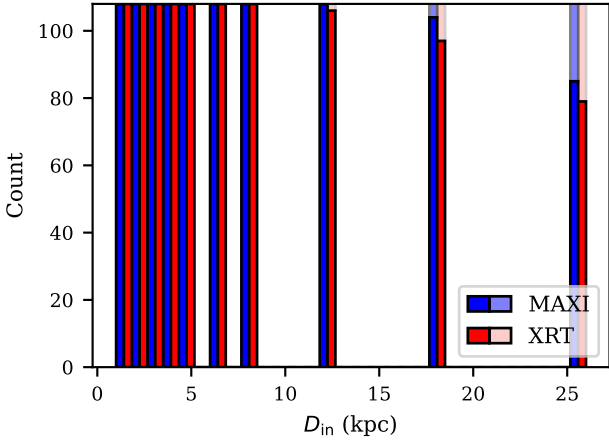


Figure 11. This plot shows a stacked histogram of the availability of distance estimations that are within 10 % of the input distance for the subset of simulations with; disc-to-total flux ratio equal to 0.9, disc maximum temperature of 1 keV, non-spinning BHs, and the maximum exposure for each instrument (10 ks for *MAXI*/GSC and 5 ks for *Swift*/XRT). Note that for each D_{in} we have a total of 108 other parameter combinations other parameter combinations.

are directed toward the Bulge, and there is a correlation with the spiral arms.

4 DISCUSSION

4.1 Robustness of the soft-state distance estimations

One of the outcomes of our simulation study is that we now have a more precise understanding of the robustness of the soft-state distance estimation method developed in A24. The results of the simulations show that, in general, the method is quite robust against any variations in the eight simulation parameters (N_{H} , Γ , T , a , M , i , disc-to-total ratio, exposure time) at low distances, namely, the 1–3 kpc range. Beyond that, the robustness of the method becomes highly dependent on the specific combination of these parameters, which, given the sheer number of their possible combinations, is impossible to investigate completely. Nevertheless, we can still discuss the general findings that we observed.

One of the findings was that the method had increased robustness against variations in other parameters when the disc-to-total flux was 0.9 (see Figures 2, A4). This finding is unsurprising, as our distance estimation relies on the disc parameters, but reassuring since typically, in the soft-state, the disc flux ratios are expected to be > 0.75 (Remillard & McClintock 2006).

Furthermore, if we only look at the subset of data with a disc-to-total flux ratio equal to 0.9, we can still identify some influential values of other parameters that affect the deviations from the input distance by a substantial amount. Therefore, we can again look at the “most” robust parameter value and select the subset of the simulations with that value. Of course, we can follow this process iteratively to hone in on the most robust combinations. In particular, our simulation data show that if we follow that kind of iterative procedure, we can find that the following subset; disc-to-total flux ratio equal to 0.9, disc maximum temperature of 1 keV, non-spinning BHs, and the maximum exposure for each instrument (10 ks for *MAXI*/GSC and 5 ks for *Swift*/XRT), have very good recovery of input distances (fractional error is ≤ 0.1) for all input distances up to 12 kpc. This is

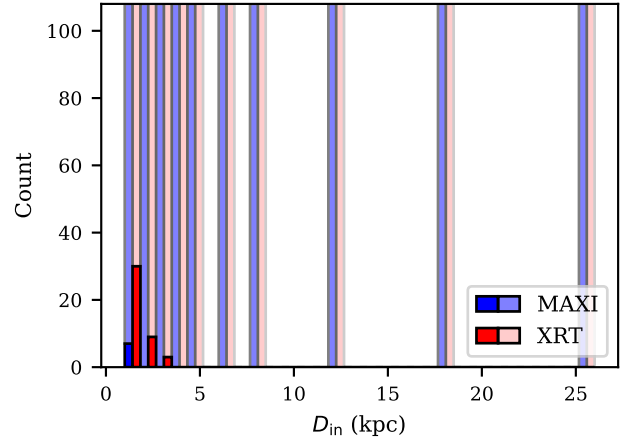


Figure 12. Same as Figure 11 but for the subset of simulations with; disc-to-total flux ratio equal to 0.2, disc maximum temperature of 0.5 keV, maximal-spinning BHs, and the minimum exposure of 0.4 ks.

independent of the values of the other parameters and the instrument (Figure 11).

We can also similarly investigate the opposite question. What are the most alarming combinations? A hint was already given when we found that in the results of the pairwise interaction effects, the simulations of $T = 0.5$ keV and $a = 0.998$ gave the highest median fractional uncertainty. Indeed, we find that, simply by picking the opposite extremum, namely, the subset with disc-to-total flux ratio equal to 0.2, disc maximum temperature of 0.5 keV, maximal-spinning BHs, and minimum exposure of 400 s. A good recovery of the input distances is almost non-existent, especially for the *MAXI*/GSC simulations (Figure 12).

These results are somewhat intuitive if we consider that accurate estimates are only obtained when the input normalisation of the *ezdiskbb* model is recovered sufficiently well from the simulated spectra. That are subject to a certain SNR binning, background subtraction, and the instrument’s fixed effective energy range. For instance, it is simple to show that by lowering the disc-to-total flux ratio and observation exposure time, the SNR binned spectra become a much lower-quality representation of the underlying input spectrum. Furthermore, it can also be shown that a lower maximum disc temperature shifts the *ezdiskbb* curve out of the detector energy range. Thus, the observed portion of the disc component becomes smaller relative to the power law, which at low normalisation (lower flux) can cause the fit to confuse between the two. Lastly, although less obvious, we argue that the maximal spin case causes the normalisation to be lower compared to the zero spin case when the other parameters in Equation 1 are kept constant and given the inclination range we considered³. This decrease in normalisation again causes the simulated spectrum to be more affected by the subsequent background “filtering” process.

In section 3, we utilised the resulting probability distribution (Figure 7) of the detector “bias” with distance to calibrate the method and mitigate some of the effects resulting from the aforementioned spectral changes. It is also evident, in hindsight, why the bias PDFs

³ We did not explicitly show how does the spin-dependant factors in Equation 1 change, since this is beyond the scope of this paper. But we refer the reader to Zhang et al. (1997) and Salvesen & Miller (2021) for a more rigorous investigation

resembled the distance inverse law, since the source emission ratio to the background emission should scale as $1/D^2$.

Based on the results of the simulations, we confirm that the soft-state distance estimate procedure developed in the A24 framework is considerably more robust when a good fit to the spectrum returns a high disc-to-total flux ratio ~ 0.9 and a maximum disc temperature $\gtrsim 1$ keV.

4.2 How does our bias-corrected observed disc radial distribution compare to the expected distribution?

In Figure 8, we overlay the theoretically expected distribution as modelled by Grimm et al. (2002, (G02)) for the Galactic LMXB population. The G02 distribution assumes that the LMXB distribution (both BH and neutron star) should follow the empirically constrained stellar distribution models of the Milky Way (Grimm et al. 2002). Therefore, they use the same three components (bulge, disc, and spheroid) to model the standard stellar distribution (Bahcall & Soneira 1980; Dehnen & Binney 1998). However, they modify it to better fit the observed LMXB population by changing the vertical scale height of the disc component and re-weighting the relative ratio between the disc, and the spheroid masses (Grimm et al. 2002). It is important to note that this expected distribution is obtained by analysing both BH and neutron stars, but our sample does not include neutron star LMXB. However, we believe that this should still be a highly insightful comparison since there would likely be a correlation between the BH-exclusive distribution and the neutron star one. This is because of two main reasons: their massive progenitors should be correlated (Fryer & Kalogera 2001), and a BH-LMXB can form by mass fallback/accretion to an initial neutron star in an LMXB (e.g. Wong et al. 2014).

We follow the same parametrisation they use in their Equations (4-6, and 10) and take the value of most parameters from Table 4 in their papers. However, we use the mass density normalisations from Atri et al. (2019), since they were not explicitly provided in G02’s Table 4. Moreover, to approximately reproduce the G02 distribution and compare it to our results, we convert the mass density to 1D probability by first assuming that the number density follows the same relation, and we then multiply by the Jacobian to transform the volume density to a radial density. Furthermore, we follow their model of the spiral structure, where they increase the disc density by a maximum of 20% utilising an angle-dependent Gaussian centred on the spiral arms locations (equation 10 in G02). We take the locations of the spiral arms model to be equally spaced (initially) from the Galactic centre. Lastly, we also included the approximate locations of the Near 3-kpc, Scutum Centaurus, and Sagittarius arms based on the most recent understanding of our Galaxy structure (Reid et al. 2019).

The figure shows good agreement with the G02 model, especially when considering the locations of the spiral structure and the decay with distance from the Galactic Centre. Nevertheless, there is a clear paucity in the near-centre sources. Based on the arguments by (Jonker et al. 2021), and our simulations (see section 4.3 and Figure 13), we think that this discrepancy might be an observational selection effect associated with the high interstellar absorption along the line of sight at low galactic heights. Alternatively, although less likely, this discrepancy could also be due to a true reduction in the number of BH-LMXBs in the region very close to the Galactic Centre. This might be because the star population very close to the centre is old, and thus the probability of having massive primaries (i.e BH progenitors) is lessened compared to the disc, which has more active regions and young populations.

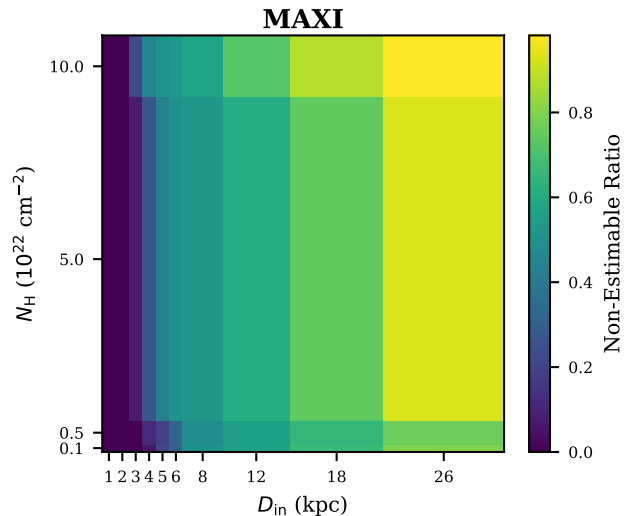


Figure 13. This 2D heatmap shows a distance mapping of the effect of N_H on the ability of the method to provide an estimated distance for the soft-state simulated spectrum and *MAXI*/GSC data. This correlates with the ability of the instrument to “detect” sources. The non-estimable ratio is calculated by taking the count of the combinations that had no distance estimates over the total combinations (54) at each $N_H - D_{in}$ grid point.

4.3 Interstellar absorption observational effect: a hidden population?

The interstellar absorption along the light-of-sight to an X-ray binary correlates with its location relative to the galactic disc. It is well established that generally the further from the galactic disc a source is observed, the lower its interstellar absorption/extinction will be (Kalberla et al. 2005; HI4PI Collaboration et al. 2016; Juvela & Montillaud 2016). Thus, the interstellar absorption can be considered as a proxy for the galactic height from the disc plane of an BH-LMXB. Furthermore, natal kicks during BH formation mean that even if a BH originated in the disc, it may end up at high galactic heights above and below the plane (Jonker et al. 2021). The determination of the galactic heights and possible associated selection effects is therefore important to constrain the natal kick distribution and, subsequently, BH formation theories.

The combination of interstellar extinction, distance from the source, and peak X-ray flux during the outburst could all conspire to produce a possible selection effect on the observed BH-LMXB population and their Galactic heights.

Our simulation study, which considers a combination of interstellar absorption, distance to the source, intrinsic properties of the source, and inclination, provides evidence that interstellar absorption plays an important role in detectability.

To show this, we used only the *MAXI*/GSC simulations since it is an actual all-sky monitoring telescope used to detect BH-LMXBs in contrast to *Swift*/XRT, which is usually used for follow-up observations. Furthermore, we limit the simulations to the ones that are close to the spectra typically observed in the soft intermediate state (i.e. the intermediate state before the soft state) in BH-LMXBs so that the source is, in principle, at or near the brightest phase during its outburst. In particular, we chose the *MAXI*/GSC simulations with a disc-to-total ratio of 0.5 and with a maximum disc temperature of 0.7 keV. Lastly, we use the 1500 s exposure time, which is very close to the average daily exposure time (~ 1400 s) for a typical single X-ray source in *MAXI*/GSC observations (Sugizaki et al.

2011). Since distance to the source and the magnitude of N_{H} are coupled in their effect on detectability, we plotted a 2D heatmap (Figure 13) that represents the degree of “undetectability” at each $N_{\text{H}}-D_{\text{in}}$ simulation grid point. The coupling effect is evident when one notices that at a very low distance of 1-2 kpc, there is virtually no effect of N_{H} on the number of detectable sources. Once the source is put at a distance larger than 3 kpc, we find that the number of detectable sources in the range of 4-6 kpc are greatly suppressed at high interstellar extinction compared to low interstellar extinction. At input distances ≥ 8 kpc, the increase in distance is the dominant effect, but interstellar extinction still plays some role in detectability. A simple comparison in the distance range 3 – 12 kpc, shows that the number of undetected sources almost doubles (161 instead of 87) at $N_{\text{H}} = 10^{23} \text{ cm}^{-2}$ compared to $N_{\text{H}} = 10^{21} \text{ cm}^{-2}$. This finding suggests that interstellar absorption is one of the main observational selection factors that can cause the low number of sources observed at very low heights ($|z| \lesssim 0.02$ kpc) relative to the Galactic disc plane due to the high interstellar absorption in that region (Willingale et al. 2013; HI4PI Collaboration et al. 2016).

We note here that the detectability of a source does not directly correspond to our synthetic spectra being good enough ($\text{SNR} > 3$) to model. This is because X-ray spectrum modelling requirements should be more stringent than a detection criterion. However, we believe that this finding should be highly correlated with the actual detectability.

4.4 Bias-corrected observed galactic heights: implications on natal kicks and BH formation channels

Now, we turn our attention back to the actual observed population. Figure 10 confirms the findings of Jonker et al. (2021), which indicate that the observed BH-LMXBs appear to be outside their expected formation region. The black holes in BH-LMXBs are expected to be correlated with regions where there is an abundance of massive progenitor stars ($20 M_{\odot} \leq M_{\text{prog}} \leq 40 M_{\odot}$) (Fryer & Kalogera 2001). These stars correlate highly with the thin-disc stellar population with a scale height of ~ 20 pc (Reid et al. 2019). It is argued in Jonker et al. (2021) that this discrepancy points to possible bias against detecting BH-LMXBs with higher masses due to observational selection effects at a lower $|z|$ than the scale height of massive stars. The bias arises from the weak natal kicks that massive BHs receive during their birth compared to the stronger ones that lower mass BHs receive (e.g. Repetto et al. 2012). The stronger natal kicks would have the effect of propelling the BHs into higher $|z|$, effectively making them easier to detect compared to their massive counterparts, which remain in the galactic plane close to the location they were formed (White & van Paradijs 1996; Jonker et al. 2021).

We found that most sources have Galactic height $|z|$ less than 1 kpc (Figure 9). This is higher than the theoretical expectations, but lower compared to the $|z|$ distribution of globular clusters, in particular, see Figure 2 in Jonker et al. (2021). Thus, our observed distribution provides yet another independent piece of evidence against the formation of BH-LMXBs in globular clusters.

If we calculate the root-mean-squared (rms)-value of z we find that when only considering *MAXI* and *Swift* sources, $z_{\text{rms}} = 969.53 \pm 447.09$ pc, On the other hand, we find $z_{\text{rms}} = 864.43 \pm 267.41$ pc, when we additionally include the *RXTE* sources. The errors in these values are estimated using a bootstrap (Efron 1979) resampling technique with 10,000 iterations. High rms Galactic height values have been argued to be evidence for high natal kick velocities during formation (e.g. Jonker & Nelemans 2004; Atri et al. 2019; Jonker et al. 2021). Since there is strong evidence that neutron star X-ray binaries,

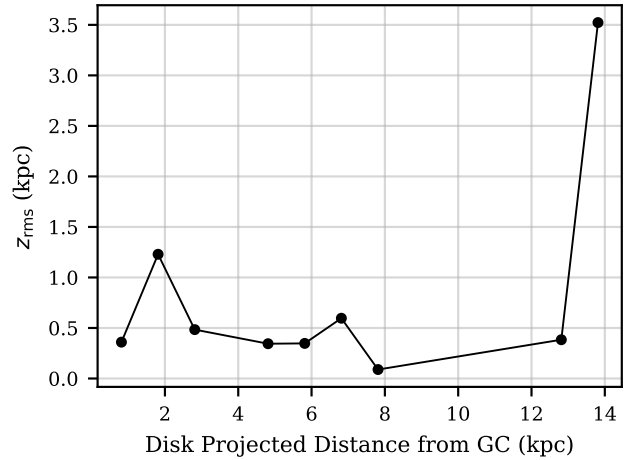


Figure 14. The observed disc radial variation of the root-mean-square (rms) height z_{rms} from the galactic midplane. The plot illustrates a roughly constant z_{rms} within ~ 10 kpc, followed by a significant flare beyond ~ 12 kpc. Compare to Figure 9 in (Repetto et al. 2017). We used the estimated median z values and 1 kpc-wide bins.

do receive high-velocity natal kicks (Hobbs et al. 2005), as evidenced by a z_{rms} of ~ 1000 pc (Brandt & Podsiadlowski 1995; van Paradijs & White 1995; White & van Paradijs 1996). However, it is important to note that this would only be valid if there were no observational biases and large differences in formation evolution between neutron stars and BHs (Repetto et al. 2017).

Furthermore, an analysis by Atri et al. (2019) of the correlation between $|z|$ and their potential kick velocity distributions (PKV) suggests that a moderate correlation exists. However, they argue that concluding velocity kicks through the $|z|$ distribution only, is not a reliable approach. As it does not explain some of the outliers they found in their data and the fact that these systems could be crossing the disc at the time of observation (Atri et al. 2019). In contrast, they state that z_{rms} should provide a good indicator of the underlying population’s natal kick magnitude, since it can, in principle, average out the time of observation bias (Atri et al. 2019).

Since we have found evidence of a hidden population at low galactic heights, we expect the currently observed rms value to be higher than the true population rms value. So, we believe that no firm conclusions should be drawn about high-velocity natal kicks solely from the current overall z_{rms} estimate.

In Repetto et al. (2017), the authors investigate the relation between the rms height and the disc-projected radial distance using different binary population synthesis models that account for different formation scenarios. These formation scenarios correspond mainly to high or low natal kicks. They found that a model with some portion of BHs receiving high-velocity natal kicks is the best match to their observations sample (Repetto et al. 2017). However, regardless of the model, they found that the radial profile of z_{rms} had an increasing trend with increased radial distance. We leveraged our estimations to probe the disc-projected radial profile of z_{rms} . We plot such graph in Figure 14 with 1 kpc-wide radial bins and using the full sample with *MAXI*, *Swift*, and *RXTE*. Our rms values are mostly around 0.5 kpc, except for the abrupt increase to ~ 3.5 kpc at a radius of ~ 13 kpc (this is only due to one source). So, our profile does not suggest a gradual z_{rms} increase as what was found using the binary population synthesis models in (Repetto et al. 2017). We caution here, that although we have a relatively large number of BH-LMXBs

compared to previous population studies, we still may not have a sufficient number of them to produce a true representation of the radial profile of z_{rms} given the 1 kpc bins, as well as the evidence for a hidden population. Furthermore, we also note that we did not consider the uncertainty of z or Galactic radius estimations arising from the distance uncertainty. A more robust method would be to perform Monte Carlo sampling from the distance distribution for each source and quantify both uncertainties in each bin. We do argue, however, that this is not likely to cause major changes in the profile given the relatively low uncertainties of the radius, and z (see Figure 10).

There has been plenty of evidence provided in favour of both high natal kicks (e.g. [Fragos et al. 2009](#); [Repetto et al. 2012, 2017](#); [Atri et al. 2019](#); [Kimball et al. 2023](#); [Mata Sánchez et al. 2025](#)), and low natal kicks (e.g. [Mandel 2016](#); [Burrows et al. 2024](#); [Janka & Kresse 2024](#); [Burdge et al. 2024](#); [Nagarajan & El-Badry 2024](#)) for BH-LMXBs. Most recently, the discovery that V404 Cygni is, in fact, a triple system ([Burdge et al. 2024](#)), provides one of the most concrete evidence for low natal kicks. As part of their analysis, the authors analysed the velocities of nearby stars and concluded that the peculiar velocity of V404 Cygni is not significantly different ([Burdge et al. 2024](#)). Given this and the tertiary discovery, they estimate the natal kick velocity as $\lesssim 5 \text{ km s}^{-1}$ ([Burdge et al. 2024](#)). Furthermore, a simulation study ([Shariat et al. 2024](#)), inspired by the V404 Cygni discovery, was conducted by utilising the state-of-art codes that incorporate triple dynamics, stellar evolution, and natal kicks. They additionally compare their triple population synthesis models with isolated binary synthesis models ([Shariat et al. 2024](#)). Their simulations strongly suggested that at least some BH-LMXBs form with very low natal kicks and that the triple formation channel is more efficient in producing BH-LMXBs than the isolated binary channel ([Shariat et al. 2024](#)). Besides this simulation study, the strong evidence of low natal kick in V404 Cygni, along with a new analysis of BH sources using the 3rd data release from *Gaia* ([Gaia Collaboration et al. 2016](#)), prompted [Nagarajan & El-Badry \(2024\)](#) in their recent investigation to favour a hybrid origin model where some BHs gain high kicks from supernova explosions, while other BHs receive minimal kicks.

As a final note, our observed z_{rms} and its uncertainties, combined with our evidence towards a hidden population in low galactic heights, seem to be most compatible with a wide range in the natal kick distribution and hence with mixed origins of BH-LMXBs, where some systems receive high kicks and some receive no or very low kicks, consistent with the most recent studies ([Shariat et al. 2024](#); [Nagarajan & El-Badry 2024](#)).

5 CONCLUSIONS

In this work, we revisited the spatial distribution of Galactic black hole low-mass X-ray binaries (BH-LMXBs) by leveraging a new and fully independent set of distance measurements obtained from soft-state and, if applicable, soft-to-hard transition X-ray spectral state modelling, developed in our previous work ([Abdulghani et al. 2024](#)). One of our goals in this current study was to mitigate systematic instrument biases stemming from variations in interstellar absorption, BH mass/spin, disc temperature, exposure time, and inclination by utilising simulations. Another goal was to gain some insight into observational selection effects through the simulation results. Finally, the main aim was to present an independent bias-corrected view of the spatial distribution of a large sample of Galactic BH-LMXBs. Our findings can be summarised as follows:

(i) **Soft-state distance method and bias correction.** Our large

grid of spectral simulations demonstrates that distance estimates derived from thermal disc-dominated states (i.e. the “soft state”) can suffer from systematic bias, especially for sources at large heliocentric distances. We have shown that the method is generally robust when the disc-to-total flux ratio is high (~ 0.9), the maximum disc temperature is $\geq 1 \text{ keV}$, and the black hole is not rotating. However, we have also found that the method can be unreliable when the disc-to-total flux ratio is low ~ 0.2 , the maximum disc temperature $\leq 0.5 \text{ keV}$, or the black hole is maximally spinning. We quantified a general bias trend approximated by an inverse-square falloff with distance. Dividing by this empirical bias distribution, we “de-biased” the distance estimations.

(ii) **Evidence for a hidden population.** After applying bias corrections, the disc-projected radial distribution of BH-LMXBs is broadly consistent with the high-mass stellar distribution models of the Milky Way ([Grimm et al. 2002](#)). Nonetheless, our simulations and observed distributions highlight the likelihood of missing systems close to the Galactic plane and in crowded fields like near the Galactic Centre, where interstellar absorption is highest. This implies that highly absorbed BH-LMXBs may remain undetected, driving a selection effect that artificially inflates the observed mean-scale height above the plane.

(iii) **Galactic height and natal kicks.** A key open question in black hole formation is whether black hole natal kicks are generally large or small (see e.g. [Repetto et al. 2017](#); [Atri et al. 2019](#); [Nagarajan & El-Badry 2024](#)). We find that the root-mean-squared (rms) height of BH-LMXBs in our sample lie within $z_{\text{rms}} \approx 0.5\text{--}1.3 \text{ kpc}$ of the Galactic plane. This is higher than the small-scale height of high-mass star-forming regions in which black holes presumably originate ($\sim 0.02 \text{ kpc}$), but still lower than the heights typically associated with globular clusters (e.g. [Jonker et al. 2021](#)). While our results cannot definitively confirm whether BH natal kicks are large, small, or both (bi-modal). We believe that our results hint that scenarios that consider a mixed origin of black hole formation with small and high kicks would be the most consistent with observations. Nevertheless, a more complete sample at small $|z|$ is needed for robust natal-kick constraints.

(iv) **Future work.** Upcoming and ongoing all-sky monitoring missions, as well as deeper follow-up in soft X-rays, will help alleviate absorption biases. Improved sensitivity at low energies will be critical, as it enhances the disc-dominated flux recovery and, thus, the accuracy of distance determination from the soft-state spectral method. Ultimately, a more complete inventory of BH-LMXBs, with well-constrained distances and spectra, will refine our understanding of black hole formation channels and the role of natal kicks in shaping Galactic black hole populations.

We emphasise that our analysis here has not included all ~ 70 ([Corral-Santana et al. 2016](#)) currently detected BH-LMXBs. Notably, systems exhibiting failed outbursts (hard-only states) were excluded. This omission introduces a potential bias towards systems more likely to transition clearly between spectral states, possibly affecting our derived spatial distributions and the inferred natal-kick conclusions. To overcome this limitation, future studies should incorporate the full diversity of outburst types by developing robust distance estimation techniques applicable even in the absence of distinct state transitions. Although the majority of BH-LMXBs do exhibit the typical behaviour that the systems included in our investigation do, including such systems could slightly modify our understanding of the Galactic distribution and potentially reveal a more comprehensive picture of BH formation mechanisms.

In general, our findings underscore the significance of selection

effects when constraining BH-LMXB demographics. While X-ray spectral fits provide a valuable method for distance estimation, the resulting distributions must be treated with care. Future dedicated surveys and follow-up programs, combined with simulations that account for realistic absorption and source evolution, will be crucial for progressing toward a comprehensive picture of black hole formation in the Milky Way.

ACKNOWLEDGEMENTS

Computational efforts were performed on the Tempest High-Performance Computing System, operated and supported by University Information Technology Research Cyberinfrastructure (RRID:SCR_026229) at Montana State University. This research leveraged the Astropy package:⁴ a community-developed core Python package and an ecosystem of tools and resources for astronomy (Astropy Collaboration et al. 2013, 2018, 2022).

DATA AVAILABILITY

The simulation study scripts and results data (SQLite database) can be found in the following repository: <https://github.com/ysabdulghani/xrb-population>. Tables of the corrected distance estimations can also be found at the same link.

REFERENCES

- Abdulghani Y., Lohfink A. M., Chauhan J., 2024, *MNRAS*, **530**, 424
- Arnaud K. A., 1996, in Jacoby G. H., Barnes J., eds, *Astronomical Society of the Pacific Conference Series Vol. 101, Astronomical Data Analysis Software and Systems V*. p. 17
- Astropy Collaboration et al., 2013, *A&A*, **558**, A33
- Astropy Collaboration et al., 2018, *AJ*, **156**, 123
- Astropy Collaboration et al., 2022, *ApJ*, **935**, 167
- Atri P., et al., 2019, *MNRAS*, **489**, 3116
- Bahcall J. N., Soneira R. M., 1980, *ApJS*, **44**, 73
- Bennett M., Bovy J., 2019, *MNRAS*, **482**, 1417
- Bradt H. V., Rothschild R. E., Swank J. H., 1993, *A&AS*, **97**, 355
- Brandt N., Podsiadlowski P., 1995, *MNRAS*, **274**, 461
- Brown G. E., Bethe H. A., 1994, *ApJ*, **423**, 659
- Burdge K. B., et al., 2024, *Nature*, **635**, 316
- Burrows A., Wang T., Vartanyan D., Coleman M. S. B., 2024, *ApJ*, **963**, 63
- Corral-Santana J. M., Casares J., Muñoz-Darias T., Bauer F. E., Martínez-Pais I. G., Russell D. M., 2016, *A&A*, **587**, A61
- Dehnen W., Binney J., 1998, *MNRAS*, **294**, 429
- Efron B., 1979, *The Annals of Statistics*, **7**, 1
- Farr W. M., Sravan N., Cantrell A., Kreidberg L., Bailyn C. D., Mandel I., Kalogera V., 2011, *ApJ*, **741**, 103
- Faucher-Giguère C.-A., Kaspi V. M., 2006, *ApJ*, **643**, 332
- Fishbach M., Kalogera V., 2022, *ApJ*, **929**, L26
- Fragos T., Willems B., Kalogera V., Ivanova N., Rockefeller G., Fryer C. L., Young P. A., 2009, *ApJ*, **697**, 1057
- Fryer C. L., Kalogera V., 2001, *ApJ*, **554**, 548
- Fryer C. L., Belczynski K., Wiktorowicz G., Dominik M., Kalogera V., Holz D. E., 2012, *ApJ*, **749**, 91
- Fryer C. L., Olejak A., Belczynski K., 2022, *ApJ*, **931**, 94
- Gaia Collaboration et al., 2016, *A&A*, **595**, A1
- Gandhi P., Rao A., Charles P. A., Belczynski K., Maccarone T. J., Arur K., Corral-Santana J. M., 2020, *MNRAS*, **496**, L22
- Gehrels N., Swift 2004, in *American Astronomical Society Meeting Abstracts*. p. 116.01
- Grimm H. J., Gilfanov M., Sunyaev R., 2002, *A&A*, **391**, 923
- HI4PI Collaboration et al., 2016, *A&A*, **594**, A116
- Haardt F., Maraschi L., 1991, *ApJ*, **380**, L51
- Haardt F., Maraschi L., 1993, *ApJ*, **413**, 507
- Heger A., Fryer C. L., Woosley S. E., Langer N., Hartmann D. H., 2003, *ApJ*, **591**, 288
- Hoang B.-M., Naoz S., Sloneker M., 2022, *ApJ*, **934**, 54
- Hobbs G., Lorimer D. R., Lyne A. G., Kramer M., 2005, *MNRAS*, **360**, 974
- Ivanova N., et al., 2013, *A&ARv*, **21**, 59
- Janka H.-T., Kresse D., 2024, *Ap&SS*, **369**, 80
- John J. A., Draper N. R., 1980, *Journal of the Royal Statistical Society. Series C (Applied Statistics)*, **29**, 190
- Jonker P. G., Nelemans G., 2004, *MNRAS*, **354**, 355
- Jonker P. G., Kaur K., Stone N., Torres M. A. P., 2021, *ApJ*, **921**, 131
- Juvela M., Montillaud J., 2016, *A&A*, **585**, A38
- Kalberla P. M. W., Burton W. B., Hartmann D., Arnal E. M., Bajaja E., Morras R., Pöppel W. G. L., 2005, *A&A*, **440**, 775
- Kara E., Alston W. N., Fabian A. C., Cackett E. M., Uttley P., Reynolds C. S., Zoghbi A., 2016, *MNRAS*, **462**, 511
- Kimball C., et al., 2023, *ApJ*, **952**, L34
- Kreidberg L., Bailyn C. D., Farr W. M., Kalogera V., 2012, *ApJ*, **757**, 36
- Lu C. X., Naoz S., 2019, *MNRAS*, **484**, 1506
- MacLeod M., Grindlay J., 2023, *arXiv e-prints*, p. arXiv:2304.09368
- Mandel I., 2016, *MNRAS*, **456**, 578
- Mata Sánchez D., Torres M. A. P., Casares J., Muñoz-Darias T., Armas Padilla M., Yanes-Rizo I. V., 2025, *A&A*, **693**, A129
- Matsuoka M., et al., 2009, *PASJ*, **61**, 999
- Mineo T., et al., 2006, *Nuovo Cimento B Serie*, **121**, 1521
- Muñoz-Darias T., Coriat M., Plant D. S., Ponti G., Fender R. P., Dunn R. J. H., 2013, *MNRAS*, **432**, 1330
- Nagarajan P., El-Badry K., 2024, *arXiv e-prints*, p. arXiv:2411.16847
- Naoz S., Fragos T., Geller A., Stephan A. P., Rasio F. A., 2016, *ApJ*, **822**, L24
- Özel F., Psaltis D., Narayan R., McClintock J. E., 2010, *ApJ*, **725**, 1918
- Pfahl E., Rappaport S., Podsiadlowski P., 2003, *ApJ*, **597**, 1036
- Podsiadlowski P., Rappaport S., Han Z., 2003, *MNRAS*, **341**, 385
- Portail M., Wegg C., Gerhard O., Martínez-Valpuesta I., 2015, *MNRAS*, **448**, 713
- Reid M. J., et al., 2019, *ApJ*, **885**, 131
- Remillard R. A., McClintock J. E., 2006, *ARA&A*, **44**, 49
- Repetto S., Davies M. B., Sigurdsson S., 2012, *MNRAS*, **425**, 2799
- Repetto S., Igoshev A. P., Nelemans G., 2017, *MNRAS*, **467**, 298
- Reynolds M. T., Miller J. M., 2013, *ApJ*, **769**, 16
- Romano P., et al., 2006, *A&A*, **456**, 917
- Salvesen G., Miller J. M., 2021, *MNRAS*, **500**, 3640
- Samland M., 1998, *ApJ*, **496**, 155
- Schwarz G., 1978, *The Annals of Statistics*, **6**, 461
- Shakura N. I., Sunyaev R. A., 1973, *A&A*, **500**, 33
- Shariat C., Naoz S., El-Badry K., Akira Rocha K., Kalogera V., Stephan A. P., Burdge K. B., Angelo I., 2024, *arXiv e-prints*, p. arXiv:2411.15644
- Shikauchi M., Tsuna D., Tanikawa A., Kawanaka N., 2023, *arXiv e-prints*, p. arXiv:2301.07207
- Siegel J. C., et al., 2023, *ApJ*, **954**, 212
- Sugizaki M., et al., 2011, *PASJ*, **63**, S635
- Tetarenko B. E., Sivakoff G. R., Heinke C. O., Gladstone J. C., 2016, *ApJS*, **222**, 15
- Timmes F. X., Woosley S. E., Weaver T. A., 1996, *ApJ*, **457**, 834
- Urquhart J. S., Figura C. C., Moore T. J. T., Hoare M. G., Lumsden S. L., Mottram J. C., Thompson M. A., Oudmajer R. D., 2014, *MNRAS*, **437**, 1791
- Wang C., Jia K., Li X.-D., 2016, *MNRAS*, **457**, 1015
- Wegg C., Gerhard O., Portail M., 2015, *MNRAS*, **450**, 4050
- White N. E., van Paradijs J., 1996, *ApJ*, **473**, L25
- Willingale R., Starling R. L. C., Beardmore A. P., Tanvir N. R., O'Brien P. T., 2013, *MNRAS*, **431**, 394
- Wilms J., Allen A., McCray R., 2000, *ApJ*, **542**, 914

⁴ <http://www.astropy.org>

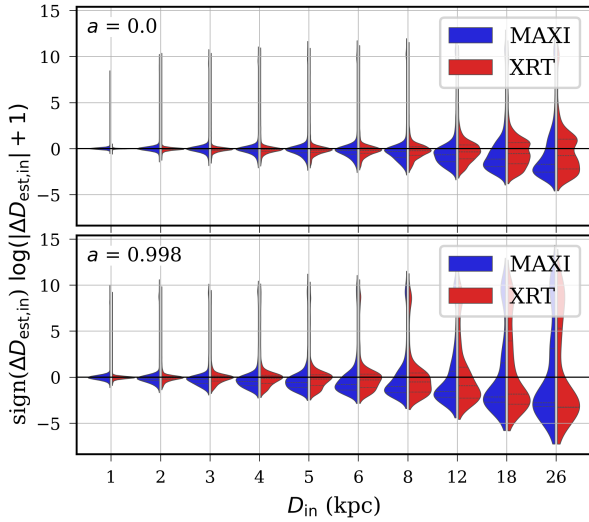


Figure A1. This shows the distributions of the log-modulus transformation of the error $\Delta D_{\text{est,in}}$ for the different BH spin α simulation values after fitting the synthetic spectra. The horizontal solid lines show where $\Delta D_{\text{est,in}} = 0$.

Wong T.-W., Fryer C. L., Ellinger C. I., Rockefeller G., Kalogera V., 2014, [arXiv e-prints, p. arXiv:1401.3032](https://arxiv.org/abs/1401.3032)
 Zhang S. N., Cui W., Chen W., 1997, *ApJ*, **482**, L155
 Zimmerman E. R., Narayan R., McClintock J. E., Miller J. M., 2005, *ApJ*, **618**, 832
 van Haaften L. M., Nelemans G., Voss R., van der Sluys M. V., Toonen S., 2015, *A&A*, **579**, A33
 van Paradijs J., White N., 1995, *ApJ*, **447**, L33

APPENDIX A: ERROR DISTRIBUTIONS

The simulation done in section 2, produced thousands of results as mentioned in that section. If you look at only one parameter value from one of the eight, there are still ~ 1000 other combinations. In this section, we explore how does the error distributions, when looking at individual parameter values, change with input distance.

As pointed out in the main text, the following transformation was applied to the deviations $\Delta D_{\text{est,in}}$:

$$\log\text{-mod}(\Delta D_{\text{est,in}}) = \text{sign}(\Delta D_{\text{est,in}}) \log(|\Delta D_{\text{est,in}}| + 1) \quad (\text{A1})$$

It is clear from Figure A1 that the black hole’s spin significantly influences the ability of the method to retrieve the input distance value accurately. The error distribution is wider for the high-spin ($\alpha = 0.998$) case. Furthermore, the peaks of the error distributions of the high-spin case for $D_{\text{in}} \geq 6$ kpc lie at considerably lower values than the zero-error line. Both *MAXI/GSC* and *Swift/XRT* results show a heavy right tail in the distribution for the high-spin case, especially at high distances. Additionally, the zero-spin simulations for *Swift/XRT* show bimodal distributions of the error compared to the high-spin case at a high distance > 12 kpc. The peaks of the *Swift/XRT* bimodal distributions are less pronounced but are closer to the zero line than the *MAXI/GSC* distributions. The zero-spin case for *Swift/XRT* simulations appears to yield peaks that are very close to the input distance, even at the highest input distances. The *MAXI/GSC* results, on the other hand, show peaks that shift lower as the input distance increases.

It can also be observed from Figure A2 that the maximum disc temperature T is another highly influential model parameter. Overall,

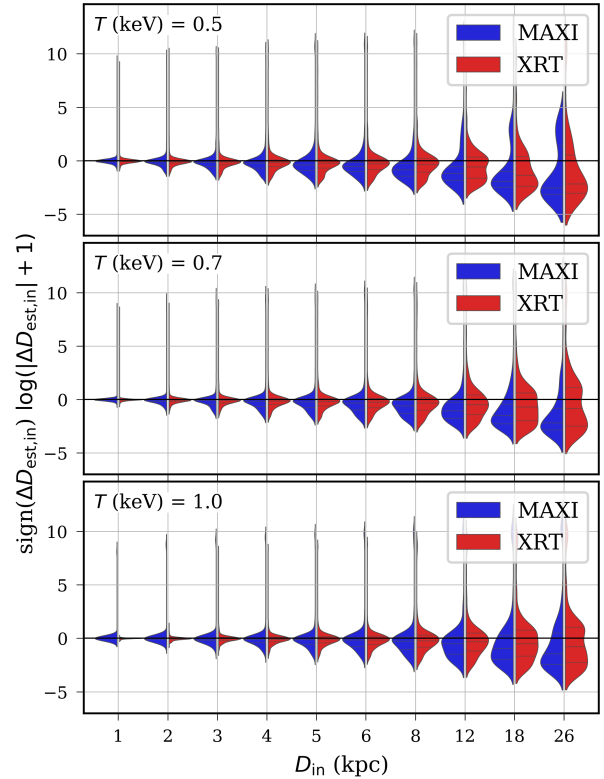


Figure A2. This shows the distributions of the log-modulus transformation of the error $\Delta D_{\text{est,in}}$ for the different maximum disc temperature T simulation values after fitting the synthetic spectra. The horizontal solid lines show where $\Delta D_{\text{est,in}} = 0$.

if the maximum disc temperature is lower, we obtain higher error values. Nevertheless, there is an exception to that trend at the 1 kpc and 2 kpc distributions, which appear to be narrower at $T = 0.7$ keV for *MAXI/GSC* only.

The distributions of the errors for the different Γ values, as shown in Figure A3, clearly reveal another high influence parameter. In particular, two major effects are evident. The distribution is wider at lower Γ and narrows as it increases. The other effect is that the entire distribution, along with its peaks, shifts lower as Γ increases. This corresponds to an increase in the magnitude of the distance underestimation. Another interesting observation is the disappearance of the very high error outliers at the highest Γ value, where input distances are ≤ 4 kpc for both instruments.

The last parameter that has a high impact on the errors is the disc-to-total ratio. As apparent from Figure A4, the peak of the distributions is much closer to the zero line for the highest ratio. This is, of course, expected given the method’s dependence on modelling the disc’s flux. The width of the distributions, however, shows an interesting pattern for *MAXI/GSC*, where it generally shrinks as the ratio increases. But for *Swift/XRT*, it is the widest at the middle ratio value.

Figure A5 shows the distribution of the log-modulus errors that resulted from the modelling of the simulated spectra for each of the grid points of the 10×4 $D_{\text{in}}-N_{\text{H}}$ grid for *MAXI/GSC* and *Swift/XRT*. As expected, the resulting error distribution is narrow when the distance is close (1-3 kpc) but widens considerably as the input distance and N_{H} increases. Overall, the distributions appear to be left-skewed, indicating that the error in the measured distances is more likely to

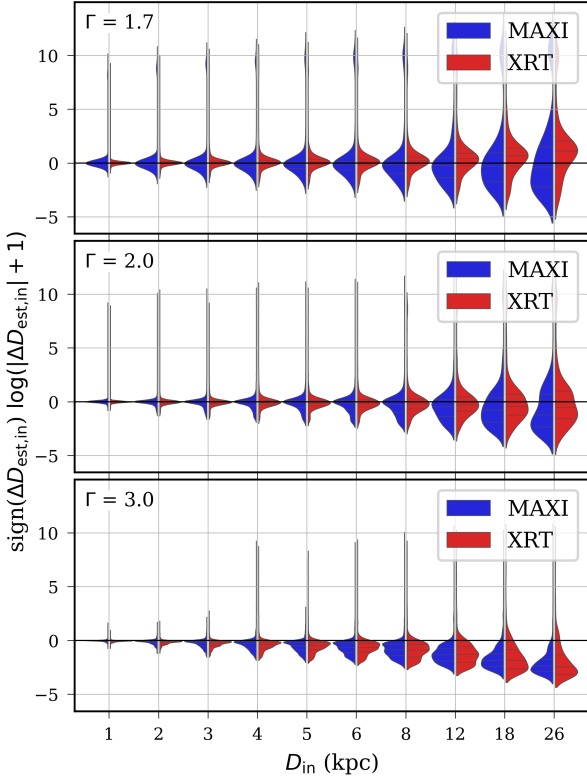


Figure A3. This shows the distributions of the log-modulus transformation of the error $\Delta D_{\text{est,in}}$ for the different power law index values Γ simulation values after fitting the synthetic spectra. The horizontal solid line shows where $\Delta D_{\text{est,in}} = 0$ is.

be an underestimation, which we already expected from the median error. There are also several outliers with very high and very low estimated distances, as evidenced by the plot scale. Comparing the *MAXI*/GSC to *Swift*/XRT results, it is clear that the lower distance distributions (1-3 kpc) are generally narrower for *Swift*/XRT results, except in the $N_{\text{H}} = 10^{23} \text{ cm}^{-2}$ case. Moreover, the distributions at higher input distances > 8 kpc show wider distributions with an apparent extra modality in the *Swift* results compared to *MAXI* results. However, their median values appear to be closer to the zero-error line.

Finally, we show the distributions for the BH mass M , disc inclination, and the exposure time in Figures A6, A7, and A8, respectively. These parameters show moderate to low effects on the distribution shape, with the changes in M having the weakest effect on the error.

APPENDIX B: ADDITIONAL INTERACTION EFFECTS FIGURES

APPENDIX C: CANDIDATE FUNCTIONS FOR FITTING THE ACCURATE DISTANCE DISTRIBUTION

APPENDIX D: MILKY WAY 2D-PLANE MAP

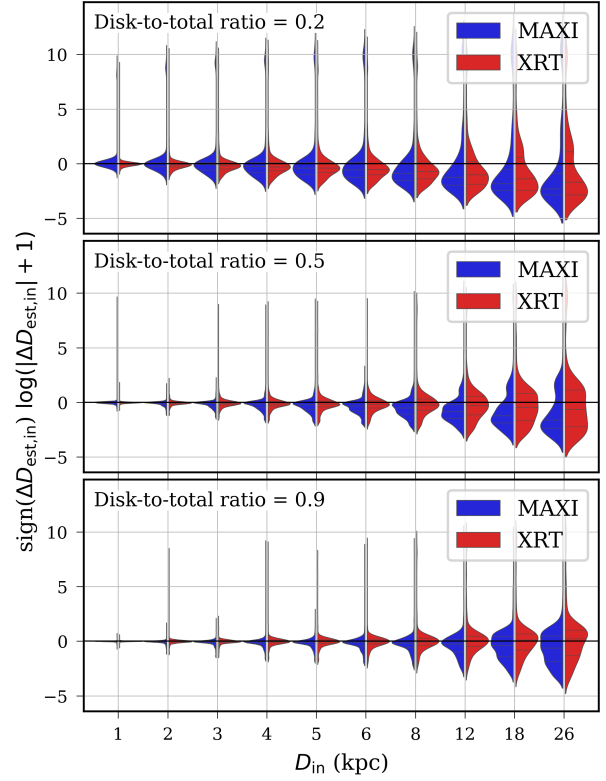


Figure A4. This shows the distributions of the log-modulus transformation of the error $\Delta D_{\text{est,in}}$ for the different disc-to-total ratio simulation values after fitting the synthetic spectra. The horizontal solid lines show where $\Delta D_{\text{est,in}} = 0$.

Table C1. Forms of the candidate probability density functions (PDFs)

Distribution	PDF Expression
Exponential Decay	$f(x) = d \exp[-a(x - c)]$
Weibull	$f(x) = d c (x - b)^{c-1} \exp[-(x - b)^c]$
Power Law with Tail (Pareto)	$f(x) = d \frac{b}{(x-c)^{b+1}}$
Cauchy	$f(x) = d \frac{2}{\pi} \frac{1}{1+(x-a)^2}$
Half Generalized Normal	$f(x) = d \frac{b}{\Gamma(1/b)} \exp[-(x - a)^b]$

Notes: The parameter d was used as an overall scaling factor.

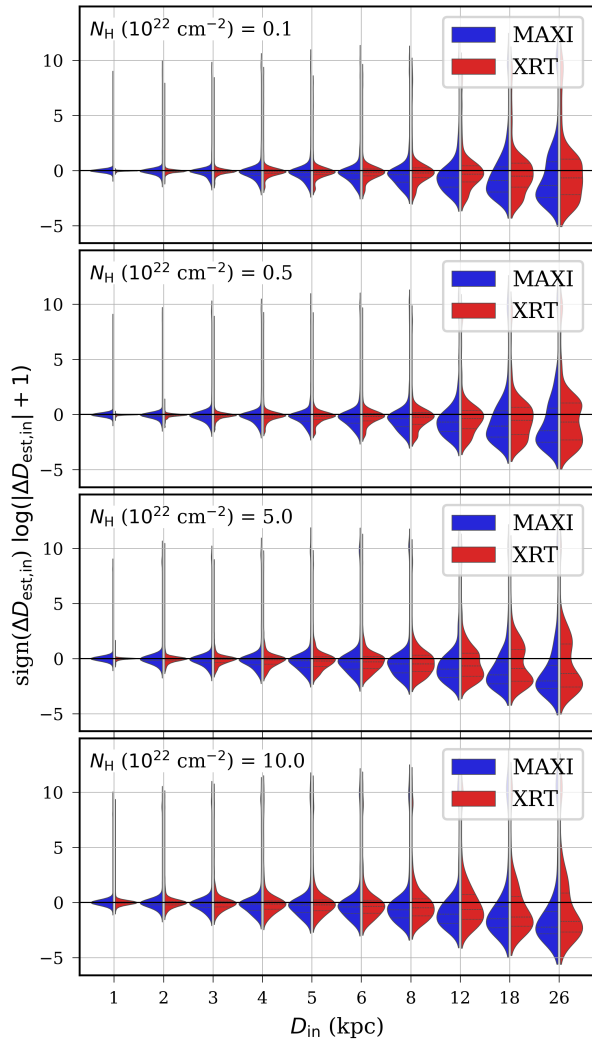


Figure A5. This shows the distributions of the log-modulus transformation of the error $\Delta D_{\text{est,in}}$ for the different N_{H} simulation values after fitting the synthetic spectra. The horizontal solid lines show where $\Delta D_{\text{est,in}} = 0$.

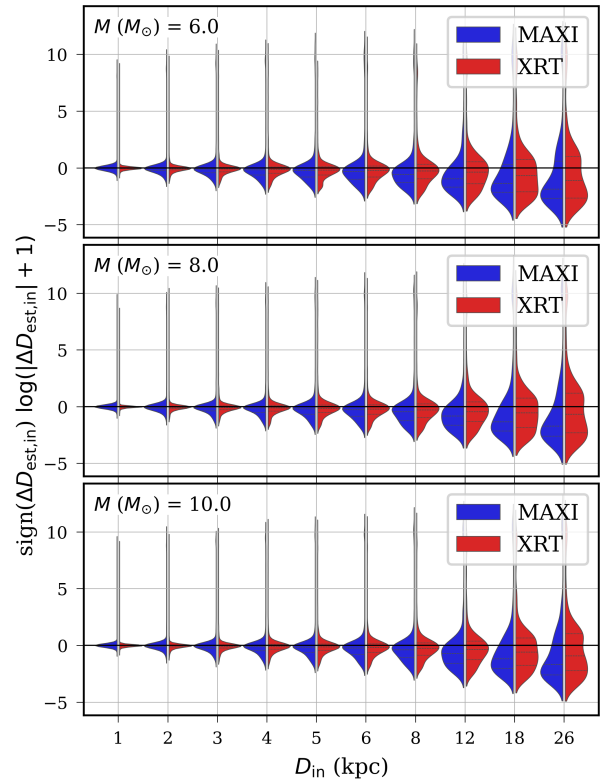


Figure A6. This shows the distributions of the log-modulus transformation of the error $\Delta D_{\text{est,in}}$ for the different BH mass M simulation values after fitting the synthetic spectra. The horizontal solid lines show where $\Delta D_{\text{est,in}} = 0$.

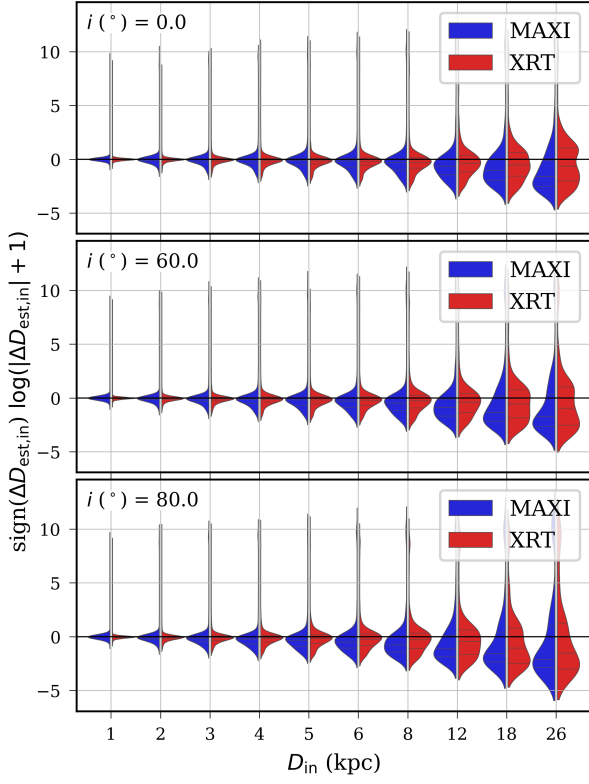


Figure A7. This shows the distributions of the log-modulus transformation of the error $\Delta D_{\text{est,in}}$ for the different disc inclination i simulation values after fitting the synthetic spectra. The horizontal solid lines show where $\Delta D_{\text{est,in}} = 0$.

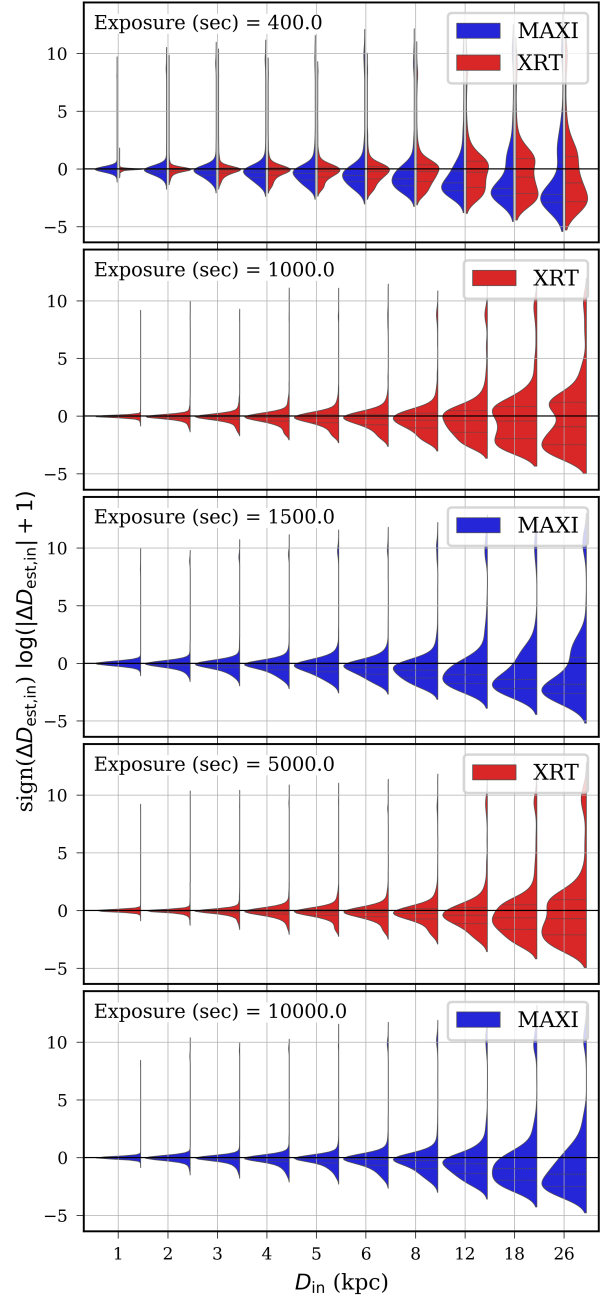


Figure A8. This shows the distributions of the log-modulus transformation of the error $\Delta D_{\text{est,in}}$ for the different exposure time simulation values after fitting the synthetic spectra. The horizontal solid lines show where $\Delta D_{\text{est,in}} = 0$.

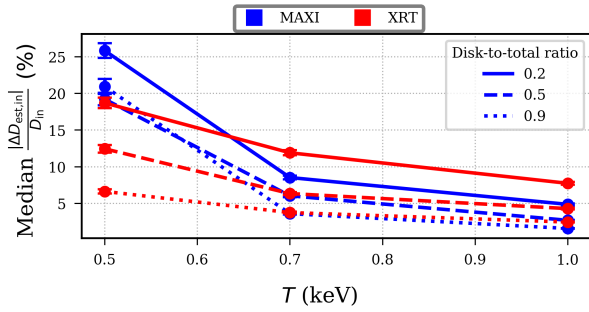


Figure B1. This figure shows pairwise interactions between T and the disk-to-total ratio. These interactions were selected via the backward stepwise BIC process.

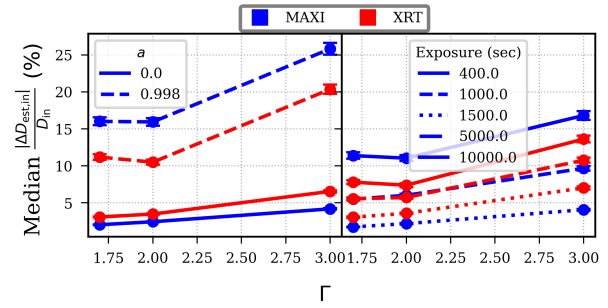


Figure B4. This figure shows pairwise interactions between the Γ and other parameters. These interactions were selected via the backward stepwise BIC process.

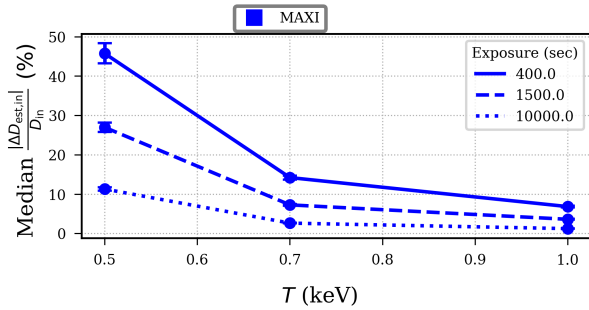


Figure B2. This figure shows pairwise interactions between T and the exposure time. These interactions were selected via the backward stepwise BIC process. This interaction was only selected for MAXI/GSC results.

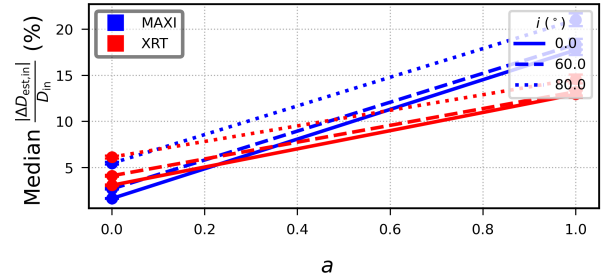


Figure B5. This figure shows pairwise interactions between a and the inclination. These interactions were selected via the backward stepwise BIC process.

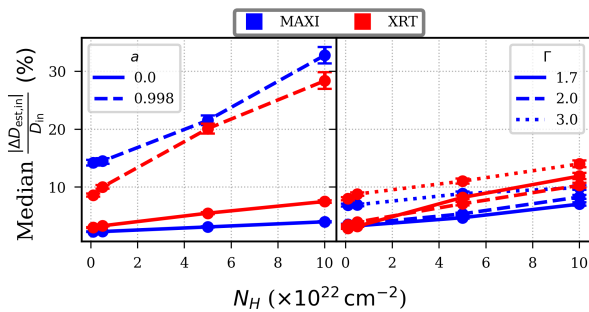


Figure B3. This figure shows pairwise interactions between N_H and other parameters. These interactions were selected via the backward stepwise BIC process.

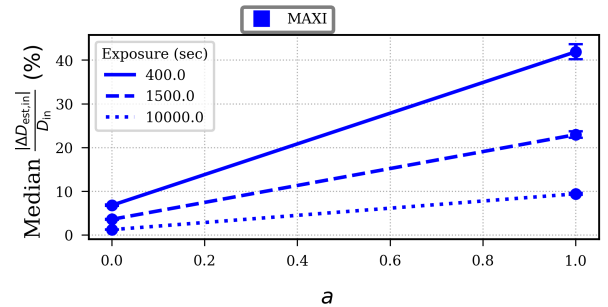


Figure B6. This figure shows pairwise interactions between a and the exposure time. These interactions were selected via the backward stepwise BIC process. This interaction was only present in the final MAXI/GSC model.

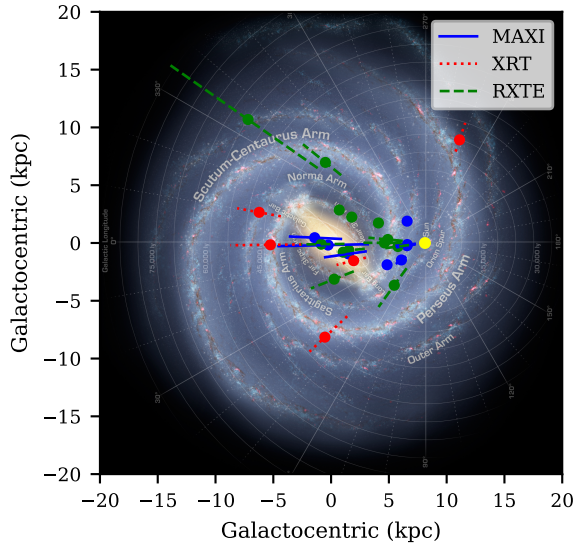


Figure D1. This figure shows the bias-corrected locations of sources in our [Abdulghani et al. \(2024\)](#) original sample. Background image: NASA/JPL-Caltech/R. Hurt (SSC/Caltech).